DOI: 10.26599/FSHW.2025.9250830

Contents lists available at SciOpen

Food Science and Human Wellness

journal homepage: https://www.sciopen.com/journal/2097-0765

China Food Publishing Co.

Baicalin Attenuates Chronic Pancreatitis through SIRT5-Mediated Nrf2 Deacetylation and JAK-STAT Pathway Modulation: Implications for Natural Product-Based Therapy

Hai Zhong[1], Bin Wu[2], Xiaoguang Wang[3], Xiaodan Yang[2*], Lingyu Hu[2*]

[1]*Emergency Department, The Second Affiliated Hospital of Jiaxing University, No.1518 North Huancheng Road, Jiaxing 314000 , Zhejiang, People's Republic of China.*

[2]*Department of Surgery, The Second Affiliated Hospital of Jiaxing University, No.1518 North Huancheng Road, Jiaxing 314000 , Zhejiang, People's Republic of China.*

[3]*Department of Surgery, Jiaxing University Affiliated Hospital, The First Hospital of Jiaxing, No.1882 South Central Road, Jiaxing 314000 , Zhejiang, People's Republic of China.*

ABSTRACT: Chronic pancreatitis (CP) is a progressive inflammatory disease marked by irreversible pancreatic fibrosis and functional decline, for which effective treatments are relatively scarce. This study explores the protective role of the dietary flavonoid baicalin (BA) in CP, with emphasis on its modulation of Sirtuin 5 (SIRT5) and associated signaling cascades. Through bioinformatics screening, nuclear factor erythroid 2-related factor 2 (Nrf2) was identified as a pivotal factor in CP pathogenesis. In rat pancreatic ductal epithelial cells (RPDECs), BA administration or Nrf2 knockdown promoted cell proliferation, inhibited apoptosis, suppressed pro-inflammatory cytokines, and facilitated Th2 polarization. In a CP rat model, BA alleviated fibrosis, reduced neutrophil accumulation, and limited collagen deposition, alongside a decline in serum levels of amylase, lipase, and trypsin. Mechanistically, multi-omics analysis demonstrated that BA activated SIRT5, leading to Nrf2 deacetylation and subsequent suppression of the JAK-STAT axis. This regulatory effect rebalanced immune responses by limiting Th1/Th17-mediated inflammation and enhancing Th2/Treg activity, thereby reducing pancreatic injury. Collectively, our findings suggest that BA mitigates CP through SIRT5/Nrf2-driven modulation of immune-fibrotic interactions, supporting its potential as a dietary agent for targeted inflammation and fibrosis control in CP.

Keywords: Chronic Pancreatitis; Baicalin; Nuclear Factor Erythroid 2-Related Factor 2; JAK-STAT Pathway; Sirtuin 5

1. Introduction

Chronic pancreatitis (CP) is a long-standing inflammatory condition of the pancreas marked by progressive fibrotic remodeling and permanent loss of exocrine and endocrine function [1-3]. Current epidemiological trends reveal a steady increase in CP incidence, often accompanied by debilitating symptoms such as persistent abdominal pain, malabsorption, and unintended weight loss—factors that substantially compromise both physical health and psychological well-being [4-6]. Over time, sustained inflammation can

***Corresponding author**
sudayangxiaodan@163.com (Xiaodan Yang);
Hulingyu07@zjxu.edu.cn (Lingyu Hu)

Received 12 March 2025
Received in revised from 13 May 2025
Accepted 25 July 2025

drive structural damage and potentially facilitate malignant transformation into pancreatic cancer [7]. Although several pharmacologic and surgical options are available, they often yield suboptimal outcomes and are frequently associated with adverse effects. Hence, exploring alternative therapeutic strategies with improved safety and efficacy remains a critical priority.

Oxidative stress and chronic immune activation are now recognized as central mediators in CP development and progression [8]. Among redox-sensitive transcription factors, nuclear factor erythroid 2-related factor 2 (Nrf2) is central to maintaining antioxidant defense and restraining inflammation. Its dysregulation in CP has been strongly linked to disease severity [9]. Nrf2 controls a network of cytoprotective genes that mitigate oxidative injury and limit inflammatory signaling [10-12]. However, emerging evidence also suggests that persistent or excessive activation of Nrf2 may paradoxically contribute to fibrogenesis [13]. In parallel, the JAK-STAT signaling cascade contributes significantly to CP pathology by facilitating immune cell infiltration and sustaining pro-inflammatory circuits [14].

Rooted in the Traditional Chinese Medicine (TCM) doctrine of “medicine and food homology,” a concept recorded as early as the *Huangdi Neijing Suwen* [15], natural compounds have long been used for disease prevention and treatment. Baicalin (BA), a major flavone glycoside extracted from *Scutellaria baicalensis*, has been shown to possess potent antioxidant, anti-inflammatory, and immunomodulatory activities [16]. A growing body of research supports BA's therapeutic potential in various disease models, citing its antibacterial, antiviral, anti-tumor, neuroprotective, and metabolic regulatory functions [17, 18]. Moreover, its benefits in managing chronic conditions—including liver dysfunction, cardiovascular disease, diabetes, and systemic inflammation—have been attributed to its capacity to modulate the gut microbiota, suppress inflammatory mediators, and enhance antioxidant enzyme activity [19, 20].

Despite accumulating evidence of BA's therapeutic promise in CP and other chronic diseases [19, 21], its underlying mechanisms, especially those involving Sirtuin 5 (SIRT5) and Nrf2, remain poorly understood. SIRT5, a mitochondrial lysine deacylase implicated in metabolic regulation, has recently gained attention for its involvement in immune regulation and inflammatory disorders [22-24]. Clarifying how BA interfaces with the SIRT5/Nrf2 axis could provide mechanistic insight and strengthen the rationale for its clinical application.

In this study, we integrate bioinformatics approaches with cellular and animal models to systematically elucidate how BA regulates CP. *In vitro* assays—including cell counting kit-8 (CCK-8), flow cytometry (FCM), and reverse transcription quantitative polymerase chain reaction (RT-qPCR)—were employed using rat pancreatic ductal epithelial cells (RPDECs) to explore the biological responses induced by BA. An in vivo CP model was used to validate the protective effects of BA on pancreatic architecture, immune infiltration, and fibrotic severity. Multi-omics profiling was further leveraged to identify molecular targets and signaling alterations involved in BA-mediated effects.

This study investigates how BA influences immune regulation and fibrotic remodeling in CP, particularly through SIRT5-mediated acetylation of Nrf2. This investigation not only contributes to a deeper

understanding of CP pathophysiology but also highlights BA as a promising candidate for dietary-based intervention. Ultimately, this research lays the groundwork for future translational studies and offers new insights for improving clinical outcomes in CP patients.

2. Materials and Methods

2.1 Ethical Statement

All procedures involving animals followed institutional and national ethical standards, with protocol approval from the Institutional Animal Care and Use Committee (IACUC) of JUMC (No. JUMC2024-109). Humane care was ensured throughout the study, and euthanasia was conducted with ether anesthesia at endpoint.

2.2 Single-Cell RNA Sequencing (scRNA-seq) Analysis of Human Pancreatic Tissue from CP Patients

Data Acquisition: scRNA-seq datasetwere retrieved from the Gene Expression Omnibus (GEO) under accession number GSE165045 (http://www.ncbi.nlm.nih.gov/geo/). This dataset includes pancreatic tissues from three healthy donors (collected postmortem), five patients with hereditary pancreatitis, and four patients with idiopathic pancreatitis. For this analysis, we selected samples from three healthy individuals (Control group, n = 3; GSM5025045, GSM5025046, GSM5025047) and three idiopathic CP patients (CP group, n = 3; GSM5025048, GSM5025049, GSM5025050).

Data Processing and Clustering: All analyses were implemented in R utilizing the Seurat package. Quality control (QC) was adopted to retain cells with 200–5000 detected features (nFeature_RNA) and mitochondrial content below 20% (percent.mt < 20). We identified the top 2000 highly variable genes for downstream analysis. Principal component analysis (PCA) was conducted on these genes to reduce dimensionality. Based on the ElbowPlot, the first 20 principal components were retained. We then applied the FindClusters function (resolution = 1) to identify cell clusters. For visualization, t-distributed stochastic neighbor embedding (t-SNE) was used to project cells in two-dimensional space. Marker genes were detected with Seurat; subsequent cell-type annotation relied on lineage markers curated from CellMarker. Intercellular communication networks were inferred using the CellChat package.

Differential expression analysis between control and CP groups was implemented utilizing the Limma package. Genes with $|\log_2 FC| > 1$ and $P < 0.05$ were deemed significant. To narrow down CP-related genes, we queried the GeneCards database (https://www.genecards.org/) utilizing the keyword “chronic pancreatitis,” yielding 10,714 hits. Among them, 627 genes with a relevance score > 15 were selected. These genes were intersected with the identified DEGs using the VennDiagram package.

We constructed protein-protein interaction (PPI) networks of key genes employing the STRING database (https://string-db.org/) with a confidence score cutoff of 0.700. We visualized the networks in Cytoscape (v3.5.1) and identified hub genes via the CytoHubba plugin.

2.3 Cell Culture and Treatment

We cultured RPDECs (bio-132359, Biobw) in DMEM (11965092, Thermo Fisher, USA) enriched with 10% fetal bovine serum (FBS, 10100147C, Thermo Fisher), 1% penicillin-streptomycin (15140163, Thermo Fisher), and 1% L-glutamine. Cells were maintained at 37°C with 5% CO_2 in a humidified incubator (Heracell™ Vios 160i CR, Thermo Scientific™). We passaged the cells when they reached 80-90% confluence.

To induce an *in vitro* pancreatitis model, we exposed RPDECs to 100 nM cerulein (HY-A0190, MedChemExpress, USA) for 24 hours.

BA treatment: We prepared a 20 mM stock solution of BA (HY-N0197, MedChemExpress) in sterile PBS. After seeding RPDECs into 6-well plates at 1×10^6 cells/well (three replicates/group) and allowing attachment overnight, we treated the cells with 0, 50, 100, or 200 μM BA for 24 hours.

We divided the experimental groups as follows: BA group: 200 μM BA only, BA + Et group: 200 μM BA + 10 μM SIRT5 inhibitor Et-29 (NRD167, AbMole, USA), and BA + RTA group: 200 μM BA + 20 nM Nrf2 activator RTA-408 (S7672, Selleck, USA).

For co-culture, we seeded RPDECs and rat T cells (KMCC-002-118, COWELDGEN SCIENTIFIC) in a 1:1 ratio into the lower and upper chambers of Falcon* Cell Culture Inserts (Corning, NY), respectively.

2.4 Lentiviral Transfection

Sangon Biotech (Shanghai, China) synthesized and packaged the lentiviral constructs for gene overexpression and silencing. We used pHAGE-puro plasmids along with pSPAX2 and pMD2.G (Addgene #118692, #12260, #12259) for overexpression, and pSuper-retro-puro with gag/pol and VSVG (Addgene #113535, #14887, #8454) for knockdown. To generate viral particles, we co-transfected these plasmids into HEK293T cells (Bio-72947, Biobw) employing Lipofectamine 2000 (11668030, Thermo Fisher). After 48 and 72 hours, we collected the supernatants, filtered them via a 0.45 μm membrane, centrifuged to concentrate viral particles, and determined viral titers.

We seeded HEK293T cells into 6-well plates at 1×10^5 cells/well and, after 24 hours, added lentiviral solution (MOI = 10, ~5×10^6 TU/mL) containing 5 μg/mL polybrene (TR-1003, Merck, USA). Four hours post-infection, we diluted the polybrene by adding an equal volume of fresh medium and replaced the medium after another 24 hours. To select stable transductants, we cultured the infected cells in puromycin (E607054, Sangon Biotech) at increasing concentrations (2 to 10 μg/mL). We verified transduction efficiency utilizing Western blot (WB) and RT-qPCR. Among the designed shRNA sequences (listed in Table S1), we selected the most effective for downstream experiments.

We defined cell groups as follows: sh-NC RPDECs (Nrf2 knockdown control cells); sh-Nrf2 RPDECs (Nrf2 knockdown cells); oe-NC RPDECs (Nrf2 overexpression control cells); oe-Nrf2 RPDECs (Nrf2 overexpression cells).

2.5 RT-qPCR

We extracted total RNA from tissues and cultured cells using the TRIzol reagent kit (A33254, Thermo Fisher, USA). Using the PrimeScript RT reagent kit (RR047A, Takara, Japan), we synthesized cDNA from

the isolated RNA. We then performed RT-qPCR with the SYBR® Premix Ex Taq™ II kit (DRR081, Takara, Japan) on an ABI7500 system (Thermo Fisher, USA). We used GAPDH as the internal control and calculated relative mRNA expression using the $2^{-\Delta\Delta Ct}$ method. All samples were tested in triplicate, with three biological replicates per group. Primer sequences are summarized in Table S2.

2.6 WB

We lysed tissues and cells in radio immunoprecipitation assay buffer containing 1% phenylmethanesulfonyl fluoride (P0013B, Beyotime, China) to extract total protein. After centrifugation, we quantified protein concentrations using a bicinchoninic acid (BCA) kit (P0011, Beyotime) and adjusted them to 1 μg/μL. Samples (100 μL each) were denatured at 100°C for 10 minutes and stored at -80°C. We prepared 8-12% sodium dodecyl sulfate-polyacrylamide gel electrophoresis (SDS-PAGE) gels in light of the target protein size and loaded 50 μg of protein per lane. Electrophoresis was carried out at 80 V (stacking) and 120 V (separating) for 2 hours. We then transferred proteins to polyvinylidene fluoride (PVDF) membranes (1620177, Bio-Rad, USA) using a wet-transfer system (250 mA, 90 minutes).

We blocked the membranes with 5% skim milk in TBST for 1 hour, then incubated them overnight at 4 °C with primary antibodies (Table S3). After three 10-minute washes in TBST, we added HRP-conjugated secondary antibodies (goat anti-rabbit IgG, ab6721; goat anti-mouse IgG, ab205719; both 1:5000, Abcam) and incubated for 1 hour at ambient temperature. Following additional washes, we developed the membranes utilizing enhanced chemiluminescence reagent (1705062, Bio-Rad) and visualized the bands with the ImageQuant LAS 4000C system (GE). GAPDH, β-actin, or β-catenin served as internal controls. We quantified relative protein levels by normalizing target band intensities to those of the reference proteins.

2.7 Cell Viability Assay (CCK-8)

We assessed RPDEC viability using the CCK-8 kit (C0041, Beyotime, Shanghai, China). After enzymatic digestion, cells were resuspended and adjusted to a density of 1×10^5 cells/mL. We seeded 100 μL of the suspension into each well of a 96-well plate and allowed the cells to adhere overnight. At 12, 24, 36, and 48 hours, we added 10 μL of CCK-8 reagent to each well and incubated the plates at 37°C with 5% CO_2 for 2 hours. Absorbance was recorded at 450 nm utilizing a microplate reader (BioTek, USA). Cell viability was calculated as:

$$Cell\ viability\ (\%)=\left(\frac{OD_{sample}-OD_{blank}}{OD_{control}-OD_{blank}}\right)\times100$$

Where, OD_{sample}: absorbance of the treated group; $OD_{control}$: absorbance of untreated control cells; OD_{blank}: background absorbance of medium with CCK-8 but without cells.

2.8 5-ethynyl-2'-deoxyuridine (EdU) staining

To evaluate proliferative activity, we performed EdU staining employing the EdU Cell Proliferation Kit (ST067, Beyotime, China). RPDECs were plated into 24-well plates at 1×10^5 cells/well with three replicates per group. After cell adhesion, we added EdU to the culture medium at a final concentration of 10 μM, followed by 2-hour of incubation at 37°C. We fixed the cells with 4% paraformaldehyde (PFA) in PBS for

15 minutes, permeabilized with 0.5% Triton X-100 for 20 minutes, and rinsed with PBS containing 3% BSA. Each well was then incubated with 100 μL of click chemistry reaction buffer for 30 minutes (dark condition). Nuclei were counterstained with DAPI for 5 minutes. We mounted the coverslips and visualized 6-10 randomly selected fields via a fluorescence microscope (FM-600, Pudan Optical, China). The EdU-positive rate was determined as: EDU labeling rate (%) = [EDU^+ cells / (EDU^+ + EDU^- cells)] × 100%.

2.9 Apoptosis Detection in RPDECs

We assessed apoptosis in RPDECs utilizing the Annexin V-FITC/PI kit (C1062L, Beyotime). Cells (1×10^6 per well) were cultured in 6-well plates, treated accordingly, then harvested and resuspended in 195 μL binding buffer. After adding 5 μL Annexin V-FITC and 10 μL PI, we incubated the samples at ambient temperature (dark condition) for 15 minutes. Flow cytometry (BD FACSCalibur) was performed within 20 minutes. Early and late apoptotic cells were identified as Annexin V^+/PI^- (Q1-LR) and Annexin V^+/PI^+ (Q1-UR), respectively, and their sum was used to calculate total apoptosis.

To further assess both apoptotic and necrotic cells, Hoechst 33342/PI double staining was performed using a commercial kit (BL116A, Biosharp, China). Cells were incubated for 10 minutes in PBS containing Hoechst 33342 (5 μg/mL) and PI (2 μg/mL). After staining, fluorescence was visualized utilizing an Axio Observer D1 microscope (Carl Zeiss, Göttingen, Germany). Hoechst 33342 stained all nuclei (blue), whereas PI selectively marked compromised cell membranes of necrotic or late-apoptotic cells (red), enabling discrimination between viable, apoptotic, and necrotic populations.

2.10 FCM Analysis

We performed FCM to characterize immune cell subsets in pancreatic tissue. After excision, the pancreatic tissue was rinsed with DPBS and transferred into a digestion buffer containing 0.2% (w/v) collagenase type II and 0.2% (w/v) phosphatase (D4693, Sigma). We incubated the samples at 37°C for 4 hours on a horizontal shaker set at 150 rpm. After enzymatic dissociation, we passed the suspension through a 70 μm nylon cell strainer to remove debris and centrifuged it at 400 × g for 5 minutes. We resuspended the pellet in 20 mL of α-MEM (SH30265.01, Hyclone) and layered it onto 20 mL of 75% Percoll (P1644, Sigma-Aldrich) in a 50 mL conical tube. Centrifugation was carried out at 450 × g for 20 minutes. From the interface, we collected the mononuclear cell layer (~5 mL), diluted it 1:10 with α-MEM, and centrifuged again at 400 × g for 5 minutes. The resulting cells were washed, counted, and resuspended in PBS supplemented with 0.5% BSA and 2 mM EDTA for surface marker staining. For macrophage analysis in synovial samples, we enzymatically dissociated the cells using trypsin, centrifuged at 400 × g for 5 minutes, and washed the pellet three times with PBS before proceeding to staining.

We stained cell suspensions with the following fluorescently labeled antibodies: anti-CD3-PE, anti-CD4-FITC, anti-CD8-PE (Abcam, UK; catalog nos. ab157300, ab239230, ab95526), and anti-CD25-APC, anti-IFN-γ-DB1, anti-IL4-OX81, anti-IL17-APC, anti-Foxp3-PE (Thermo Fisher, USA; 17-0390-82, 50-7310-80, 50-7045-82, 17-7177-81, 12-5773-82). Following incubation, we analyzed the stained cells using a BD FACSCalibur flow cytometer.

2.11 Enzyme-Linked Immunosorbent Assay (ELISA)

We quantified inflammatory cytokines—interleukin-6 (IL-6), tumor necrosis factor-alpha (TNF-α), IL-1β, IL-10, and TGF-β—in rat serum and cell supernatants using commercially available ELISA kits (Cat. Nos. E-EL-R0015, E-EL-R2856, E-EL-R0012, E-EL-R0016, E-EL-R1015; Elabscience, Wuhan, China). Briefly, we added standards and experimental samples to antibody-coated wells and incubated them to allow target protein binding. After thorough washing, we added biotinylated detection antibodies, followed by an HRP-conjugated reagent. Upon final washing, we introduced 3,3',5,5'-Tetramethylbenzidine (TMB) substrate to initiate color development, which was halted by a stop solution, changing the color from blue to yellow. We measured absorbance at 450 nm utilizing a microplate reader. All readings were blank-corrected prior to data analysis.

2.12 Immunofluorescence Staining

Cell Preparation: We seeded RPDECs on sterile coverslips and allowed them to adhere and proliferate under standard culture conditions. Cells were rinsed with PBS and fixed in 4% PFA for 20 minutes at ambient temperature. Following fixation, we washed the coverslips three times with PBS to complete cell preparation.

Tissue Preparation: Fresh tissue samples were fixed in 4% PFA for 24 hours, followed by dehydration in graded ethanol and clearing with xylene. After paraffin embedding, we sectioned the tissue into 4-5 μm slices utilizing a microtome. Slices were floated in a 40°C water bath and mounted onto glass slides. We dewaxed the slides with two 5-minute xylene washes, followed by sequential hydration in 100%, 95%, and 70% ethanol (5 minutes each). After rinsing in distilled water, we performed antigen retrieval by microwaving slides in citrate buffer (pH 6.0) until boiling, then allowing them to cool to room temperature. We washed the sections three times with PBS (5 min each), fixed them in -20°C methanol for 30 minutes, and washed again with PBS. Permeabilization was carried out using 0.1% Triton X-100 (P0096, Beyotime) for 15 minutes, followed by PBS rinses.

We blocked nonspecific binding with BSA for 30 minutes at ambient temperature. We then incubated the sections with the following primary antibodies: rabbit anti-Nrf2 (ab313825, 1:500, Abcam, UK) and mouse anti-α-SMA (14-9760-82, 1:100, Thermo Fisher, USA) at 37°C for 1 hour. After three PBS washes, we counterstained the nuclei using DAPI (C1002, Beyotime) for 10 minutes and washed the slides again. We mounted the slides with antifade mounting medium (20 μL per slide) and captured images via a laser scanning confocal microscope (Leica, CH). We analyzed fluorescence employing ImageJ Pro Plus 6.0 software. For each group, we calculated the average fluorescence area across six random 40× fields. Quantitative results were expressed as mean values and used for statistical comparisons. All experiments were repeated independently in triplicate.

2.13 Establishment of the CP Rat Model

We used eight-week-old male Sprague-Dawley rats (180-200 g, strain 101; Beijing Vital River Laboratory Animal Technology Co., Ltd., China), housed under SPF conditions with a 12-hour light/dark cycle, controlled humidity (60%-65%), and ambient temperature (22-25°C). Animals had free access to food

and water. After a week of acclimatization period, all experimentations were carried out following approval from the Institutional Animal Ethics Committee.

To manipulate Nrf2 expression, we administered 50 μL of lentiviral vectors (1×10^{11} PFU) via tail vein injection 48 hours before CP induction. The rats were allocated into four groups (n=6 per group): sh-NC (silencing control), sh-Nrf2 (Nrf2 knockdown), oe-NC (overexpression control), and oe-Nrf2 (Nrf2 overexpression). Two weeks after CP induction, rats were euthanized, and pancreatic tissues were harvested for further analyses.

Establishment of CP Rat Model: We induced CP by intravenously injecting dibutyltin dichloride (DBTC; 8 mg/kg, Cat. 205494, Merck, USA), dissolved in ethanol and mixed with glycerol in a 1:2:3 ratio. Each rat received 200 μL of this solution via tail vein under brief restraint. Injections were repeated every three days for two weeks. We monitored rats for clinical signs of CP, such as lethargy, reduced appetite, weight loss, ruffled fur, and diarrhea. Control animals received the same volume of vehicle solution without DBTC.

Following successful model establishment, rats were randomized into control group (healthy rats injected with 100 μL PBS via the tail vein), CP model group (CP-induced rats injected with 100 μL PBS), BA1 group (CP rats treated with 100 mg/kg BA in 100 μL PBS), BA2 group (CP rats treated with 200 mg/kg BA), and BA3 group (CP rats treated with 400 mg/kg BA) (n=6 each). All treatments were delivered via daily tail vein injection for 28 consecutive days. Upon completion of treatment, we collected serum samples and euthanized the animals. To quantify ascites, we placed sterile gauze in the peritoneal cavity for 5 minutes and measured the weight difference before and after. Pancreatic tissues were collected for subsequent biochemical and histopathological analyses [25-27].

To explore the underlying mechanism, we further grouped CP rats as follows: PBS group (received 100 μL PBS), BA group (received 400 mg/kg BA), BA+Et group (co-administered 400 mg/kg BA and 100 mg/kg SIRT5 inhibitor Et-29), and BA+RTA group (co-administered 400 mg/kg BA and 100 mg/kg Nrf2 activator RTA). We administered all treatments via tail vein injection [28, 29].

2.14 Hematoxylin and Eosin (H&E) Staining

To evaluate histopathological alterations in rat pancreatic tissue, H&E staining was conducted using a commercial kit (C0105S, Beyotime, Shanghai, China). Tissue samples were first fixed in 4% PFA (P0099, Beyotime), followed by sequential dehydration, clearing, and paraffin embedding. Sections were sliced at 5 μm thickness with a microtome, baked, deparaffinized, and rehydrated. Hematoxylin was applied for nuclear staining, followed by rinsing and eosin staining for cytoplasmic contrast. Sections underwent acid-alcohol differentiation in 70% hydrochloric ethanol, dehydration, clearing, and final mounting with neutral resin. Morphology of the pancreas and major organs (heart, liver, spleen, kidney) was examined under a light microscope. Slides were scanned using the Aperio ScanScope CS system (Leica Biosystems, Germany) for digital imaging.

2.15 Histopathological Scoring

To assess pancreatic pathology, ascitic fluid was absorbed using sterile cotton pads, and the weight change before and after absorption was recorded. Fixed pancreatic tissues were processed for paraffin embedding and H&E staining. Two independent observers, blinded to the experimental groups, evaluated the stained sections using the modified Spormann scoring criteria (Table S4). Lesion severity, inflammatory infiltration, and tissue necrosis were quantitatively scored. Additionally, serum amylase (AMY) activity was determined via iodine-starch chromatography. Levels of pro-inflammatory cytokines (TNF-α and IL-6) were measured utilizing ABC-based ELISA kits, providing a multiparametric overview of pancreatic inflammation and injury.

2.16 Terminal Deoxynucleotidyl Transferase dUTP Nick End Labeling (TUNEL) Assay for Apoptosis Detection

Cellular apoptosis in pancreatic tissue was examined utilizing the TUNEL assay kit (C1088, Beyotime, Shanghai, China). After fixation in 4% PFA for 30 minutes, sections were washed three times with PBS and permeabilized using 0.3% Triton X-100 in PBS for 3 minutes. Following two additional PBS rinses, 50 μL of TUNEL reaction mixture was added to each section, and samples were incubated at 37°C in the dark for 1 hour. After washing, cell nuclei were counterstained with DAPI (10 μg/mL) for 10 minutes. Slides were mounted using anti-fade medium and imaged using a fluorescence microscope. Apoptotic cells were identified by red Cy3 fluorescence (excitation: 550 nm; emission: 570 nm). The apoptotic index was calculated from six random fields per sample utilizing Image-Pro Plus 6.0 software.

2.17 Masson Staining

To evaluate pancreatic fibrosis, 4 μm paraffin-embedded sections were subjected to Masson's Trichrome staining using a commercial kit (DC0032, Leagene Biotechnology, Beijing, China). We deparaffinized and rehydrated the sections, stained them with hematoxylin for 5-10 minutes, and then briefly differentiated them in acidic ethanol (5-15 seconds). Subsequent bluing was performed in Masson's blue solution for 3-5 minutes. Sections were then treated with Ponceau red for 5-10 minutes, phosphomolybdic acid for 1-2 minutes, and aniline blue for 1-2 minutes. Finally, samples were dehydrated in graded ethanol, cleared with xylene, and mounted. Fibrotic areas were visualized under an Olympus BX51 microscope (200× magnification; Olympus, Tokyo, Japan) and quantified utilizing ImagePro Plus 6.0 software.

2.18 Sirius Red Staining

Sirius Red staining was used to further assess collagen deposition in pancreatic tissue. After euthanasia, 6 μm sections were deparaffinized and rehydrated. Sections were stained with hematoxylin for 10-20 minutes, differentiated in acid alcohol for 10 seconds, and rinsed in tap water for 10 minutes. Next, slides were incubated in Sirius Red solution (365548-5G, Sigma-Aldrich, USA) at ambient temperature for 1 hour. After washing, tissues were dehydrated, cleared, and mounted. For semi-quantitative analysis, three sections per rat were selected, and five random fields per section were imaged under high magnification. Fibrosis was quantified as the positive area using Image-Pro Plus 6.0.

2.19 Detection of Serum AMY Activity

Serum AMY activity was determined utilizing a commercial assay kit (BC5055, Solarbio, Beijing, China), following the manufacturer's instructions. Reagents 1 and 2 were mixed and boiled to ensure full dissolution. Reagents 3A and 3B were combined and diluted to 10 mL with distilled water, then refrigerated. A starch standard (1 mg/mL) was prepared by dissolving starch in Reagent 2 and boiling. Before measurement, the spectrophotometer was preheated for 30 minutes, set to 570 nm, and calibrated with distilled water.

For sample analysis, serum was diluted 1:5 in distilled water. Each sample (100 μL) was added to a test and a control tube. The test tube received 100 μL of Reagent 1 and 50 μL of Reagent 3, while the control tube received 100 μL of Reagent 2 and 50 μL of Reagent 3. We incubated all tubes at 37°C for 10 minutes, then measured absorbance at 570 nm. Enzyme activity was determined from a standard curve, with one unit defined as the amount of enzyme that hydrolyzes 1 mg of starch per minute per milliliter of serum.

2.20 Detection of Serum Lipase Activity

Serum lipase activity was assessed using the Elabscience® LPS Colorimetric Assay Kit (E-BC-K786-M, Elabscience, Wuhan, China). All reagents were equilibrated to room temperature before use. To prepare the working solutions, Reagent 2 was diluted 1:9 with anhydrous ethanol, and this mixture was subsequently diluted 1:100 with Reagent 3. Reagent 4 was diluted 1:9 in double-distilled water, shielded from light, and used immediately.

Diluted serum samples were added to both control and measurement wells of a 96-well plate. Reagent 1 was added to control wells, while 40 μL of the working Reagent 3 solution was added to test wells. After a 5-second gentle shake, plates were incubated at 37°C for 20 minutes. Then, 150 μL of Reagent 4 was added to each well, mixed for 5 seconds, and incubated again at 37°C in the dark for 30 minutes. Absorbance at 412 nm was documented utilizing a microplate reader, and lipase activity was determined based on the kit's standard curve.

2.21 Detection of Pancreatic Trypsin Activity

Trypsin activity in pancreatic tissues was determined using a colorimetric assay kit (ab102531, Abcam, UK). Roughly 0.1 g of tissue was homogenized in cold EDTA-containing PBS, and the lysates were centrifuged at 12,000 g for 10 minutes at 4°C to remove debris. Supernatants were added to designated wells in a microplate alongside standards and positive controls. Buffer-only wells served as blanks. Trypsin inhibitor was added to both sample and positive control wells, followed by a 10-minute room temperature incubation. The reaction mix was then added, and absorbance was monitored at 405 nm at 2-3 minute intervals for up to 2 hours at 25°C. Trypsin activity was calculated based on the release of p-nitroaniline (p-NA), with absorbance values directly reflecting enzymatic activity.

2.22 Quantification of Pancreatic Myeloperoxidase (MPO) Activity

MPO activity in pancreatic tissues was quantified using a specific assay kit (BC5710, Solarbio, Beijing, China). Samples were homogenized on ice in Reagent II and centrifuged at 12,000 g for 10 minutes at 4°C. The supernatant was harvested for the assay. Samples and Reagent III were added to the respective test and control tubes, followed by the addition of the working reagent to test tubes and distilled water to controls. The tubes were incubated at 37°C for 30 minutes. Reagent VI was then added, and the mixtures were incubated at 60°C for 10 minutes. A 300 μL aliquot was transferred to a 96-well plate, and absorbance at 460 nm was recorded. MPO activity was normalized to total protein content, using the following equation:

$$\text{MPO Activity (U/mg protein)} = \Delta A \div (\varepsilon \times d) \times V_{total} \div (Cpr \times V_{sample}) \div T = 3.053 \times \Delta A \div Cpr$$

ε: Extinction coefficient of oxidized o-phenylenediamine, 11.3 mL/μmol/cm; d: Path length, 1 cm; V_{total}: Total reaction volume, 0.345 mL; Cpr: Protein concentration in the sample, mg/mL; V_{sample}: Volume of the sample added, 0.02 mL; T: Enzymatic reaction time, 30 minutes=0.5 hours.

2.23 Quantification of High Mobility Group Box 1 (HMGB1) Content

We measured HMGB1 levels in rat pancreatic tissue using a commercial ELISA kit (PH406, Beyotime, Shanghai, China). Approximately 0.1 g of tissue was homogenized in pre-chilled PBS containing EDTA, and the supernatant was collected after centrifugation (12,000 g, 10 minutes, 4°C). To generate the standard curve, we serially diluted the standard protein and incubated it for 15 minutes to ensure complete dissolution. We added 100 μL of either sample or standard to each well of a 96-well plate, sealed it, and incubated for 2 hours. After five washes, we applied 100 μL of HRP-conjugated anti-HMGB1 antibody and incubated for 1 hour, followed by another wash and addition of 100 μL HRP-labeled streptavidin for 20 minutes in the dark. Finally, we added 100 μL of TMB substrate, stopped the reaction after 15-20 minutes with 50 μL of stop solution, and immediately measured absorbance at 450 nm. HMGB1 concentrations were calculated utilizing the standard curve.

2.24 Immunohistochemistry (IHC)

Paraffin-embedded tissue sections were first equilibrated at 4°C, then baked at 60°C for 20 minutes. Slides were deparaffinized in xylene for two 10-minute cycles and rehydrated through graded ethanol series (absolute, 95%, and 70%, 5-10 minutes each), followed by a rinse in distilled water. For antigen retrieval, slides were immersed in citrate buffer (pH 6.0) and heated in a microwave for 8 minutes, then cooled to room temperature. After three washes in PBS (3 minutes each), endogenous peroxidase was blocked with 3% hydrogen peroxide for 10 minutes. Slides were rinsed again and blocked with goat serum (E510009, Sangon Biotech) for 20 minutes at ambient temperature.

Primary antibodies targeting CD3 (1:100, ab11089), CD11b (1:4000, ab133357), and F4/80 (1:5000, ab300421) (all from Abcam, UK) were applied, and slides were incubated overnight at 4°C. Following PBS washes, the HRP-conjugated goat anti-rabbit IgG secondary antibody (1:5000, ab6721, Abcam) was applied for 30 minutes at ambient temperature. The Streptavidin-Biotin Complex (SABC, P0603, Beyotime) was then added and incubated at 37 °C for 30 minutes. Color development was carried out with DAB substrate (P0203, Beyotime) for 6 minutes, followed by hematoxylin counterstaining for 30 seconds. Slides were dehydrated

through graded ethanol and cleared with xylene. Specimens were mounted utilizing neutral resin and imaged under a light microscope (BX63, Olympus, Japan). Five random high-power fields per sample were analyzed using Image-Pro Plus 6.0 to determine average optical density (OD). All assays were performed in triplicate.

2.25 Preparation of Sequencing Samples

We prepared single-cell suspensions from pancreatic tissues of PBS- and BA3-treated rats. After rinsing the tissues with ice-cold PBS to remove residual non-target material, we digested them in DMEM (11965092, Thermo Fisher) supplemented with 1 mg/mL collagenase (C2674, Sigma-Aldrich), 1 U/mL DNase I, and 10% FBS at 37°C for 30 minutes. The digested mixture was filtered through a 200-mesh strainer, and cells were collected by centrifugation at 50 g for 5 minutes at 4°C. We discarded the supernatant, resuspended the pellet in complete DMEM, and rinsed the cells twice. To remove red blood cells, we applied RBC lysis buffer (C3702, Beyotime). Apoptotic and dead cells were eliminated using the Annexin Dead Cell Removal Kit (17899, StemCell Technologies) with magnetic separation. Finally, we resuspended the viable cells in PBS for sequencing. Cell count, viability, and integrity were assessed via microscopy and FCM.

2.26 High-Throughput Transcriptome Sequencing

Transcriptome sequencing was implemented on pancreatic tissue samples from the PBS group (control, n=3) and the BA3 group (400 mg/kg BA-treated, n=3), prepared as described above. Total RNA was extracted, and its quality was validated before library construction.

RNA Purity and Integrity Validation: We assessed RNA purity using a NanoDrop ND-1000 spectrophotometer (Thermo Fisher) based on OD260/280 ratios, ensuring minimal protein and solvent contamination. RNA concentrations were quantified with the Qubit RNA Assay Kit (Q33221, Thermo Fisher, USA). Only samples with a RIN ≥ 7.0 and a 28S:18S ratio ≥ 1.5 were deemed suitable for sequencing.

We commissioned CapitalBio Technology (Beijing, China) to prepare sequencing libraries using 5 μg of total RNA per sample. Ribosomal RNA was removed with the Ribo-Zero Magnetic Kit (MRZG12324, Epicentre), and libraries were constructed using the NEBNext Ultra RNA Library Prep Kit (E7760S, NEB, USA). We fragmented RNA into ~300 bp fragments and synthesized first-strand cDNA using random hexamer primers and reverse transcriptase. For strand specificity, dUTP was incorporated during second-strand synthesis. After end repair, polyadenylation, and adaptor ligation, we applied USER Enzyme (M5508, NEB) to degrade the dUTP-labeled second strand selectively. The resulting libraries were PCR-amplified, purified, and quantified utilizing both the Agilent 2100 Bioanalyzer and the KAPA Library Quantification Kit (kk3605, Merck, USA). Paired-end sequencing was conducted on the Illumina NextSeqCN500 platform.

2.27 Transcriptome Sequencing Data Analysis

We evaluated the quality of raw paired-end reads utilizing FastQC (v0.11.8). Cutadapt (v1.18) was used to trim Illumina adapter sequences and poly(A) tails. To filter out low-quality reads, we removed those

containing over 5% ambiguous bases using a custom Perl script and retained only reads with ≥70% of bases having a Phred score >20 via the FASTX Toolkit (v0.0.13). We corrected paired-end reads using BBMap and aligned the clean reads to the rat reference genome with HISAT2 (v0.7.12).

To identify DEGs, we used the Limma package in R. Thresholds were set at $|\log_2 FC| > 1$ and $p < 0.05$. We performed Venn diagram analysis with the VennDiagram package to identify overlapping genes between groups. Functional enrichment was completed utilizing the ClusterProfiler package, covering Gene Ontology (GO) terms—Biological Process (BP), Molecular Function (MF), and Cellular Component (CC)—and Kyoto Encyclopedia of Genes and Genomes (KEGG) pathway analysis. We visualized the results utilizing bubble plots and chord diagrams.

2.28 Proteomic Sequencing and Analysis

We collected pancreatic tissues from the PBS (n = 6) and BA3 (n = 6) groups. Total protein was extracted using RIPA buffer supplemented with protease inhibitors (89900, Thermo Fisher, USA). We sonicated the samples for 30 seconds every 5 minutes, repeating the cycle three times. Protein concentrations were determined utilizing a BCA assay, and digestions were completed using trypsin (1:50, enzyme:protein) ratio for 16 hours at 37°C. Peptides were desalted using ZipTip C18, then analyzed by LC-MS/MS. The mass spectrometry workflow involved labeling peptides with iTRAQ, followed by separation on a nano-C18 column (75 μm × 15 cm, 5 μm) using a 90-minute gradient of 0.1% FA / 2% ACN (mobile phase A) and 0.1% FA / 100% ACN (mobile phase B). The LC system (Shimadzu, Japan) was coupled to a QSTAR Elite Hybrid MS (Applied Biosystems/MDS-SCIEX) with a nanospray source (New Objectives, USA). Mass spectra were collected in the range of 300-2000 m/z in positive ion mode. The top three peptide ions (charge +2 to +4) per MS spectrum were selected for fragmentation with dynamic exclusion set to 30 seconds and a mass tolerance of 30 mDa.

We used MaxQuant for protein identification and quantification. For data-independent acquisition (DIA), we employed 47 overlapping windows with 1 m/z overlap and included an iRT kit (Ki3002, Biognosys, Switzerland) for retention time calibration. We analyzed the DIA data with Spectronaut V13 (Biognosys AG), which handled both normalization and protein quantification. Welch's ANOVA was used to identify differentially expressed proteins, with $|\log_2 FC| > 1$ and adjusted $p < 0.05$ as significance thresholds. We performed WB validation using the same tissue samples. MS parameters included: (1) MS: 350-1500 m/z; resolution: 120,000; AGC target: $4e^5$; injection time: 50 ms; (2) HCD-MS/MS: resolution: 30,000; AGC target: 1e5; collision energy: 33; (3) DIA: 47 windows with 1 m/z overlap.

2.29 Statistical Analysis

All *in vitro* experiments were implemented with three biological replicates and three technical replicates per group (n = 3). *In vivo* experiments included six rats per group (n = 6). Data are reported as mean ± standard deviation (SD). We used independent-sample t-tests for comparisons between two groups. For comparisons across three or more groups, one-way ANOVA followed by Tukey's HSD test was applied. For data that violated normality or homogeneity of variance assumptions, we used the Mann-Whitney U test or the

Kruskal-Wallis H test. All statistical analyses were run in GraphPad Prism 9.5.0 and R 4.2.1. A two-tailed p-value < 0.05 was confirmed statistically significant.

3. Results

3.1 Cellular Heterogeneity in Pancreatic Tissue of CP Patients: A Bioinformatics Analysis

CP is a progressive inflammatory disorder of the pancreas, marked by persistent inflammation and fibrosis. Over time, it leads to irreversible damage to both exocrine and endocrine functions of the gland [30, 31]. Although a variety of therapeutic interventions—such as surgery, pancreatic enzyme replacement, and antioxidant supplementation—have been employed, current clinical strategies largely focus on alleviating symptoms rather than halting disease progression [30, 32].

To explore the cellular complexity of pancreatic tissue in CP, we analyzed scRNA-seq data retrieved from the GEO database, comprising samples from both CP patients (n = 3) and healthy controls (n = 3) (Figure 1A). This study aimed to identify key cellular players and signaling factors involved in CP pathogenesis.

Following quality control, normalization, and PCA, batch effects were mitigated using the Harmony algorithm. We then applied t-SNE for nonlinear dimensionality reduction based on the top 20 principal components. Clustering via t-SNE identified 13 distinct cellular clusters (Figure 1B-C). Using published literature and the CellMarker database, we annotated these clusters into five major cell types: T cells, epithelial cells, monocytes, mast cells, and B cells (Figure 1D-E). Marker gene expression was visualized to confirm the identity of these cell types, including CD3E (T cells), CK19 (epithelial cells), S100A8 (monocytes), TPSB2 (mast cells), and CD79A (B cells) (Figure 1F-G).

Next, we examined the distribution of seven cell subtypes across all six samples. Differential abundance analysis using the t-test revealed a significant increase in T and B cell populations in CP samples, accompanied by a marked reduction in epithelial cells compared to controls (Figure 1H-I).

In summary, 13 distinct cellular clusters were identified, with five major subpopulations clearly delineated. Notably, CP tissue showed an elevated proportion of T and B cells, while epithelial cells were depleted.

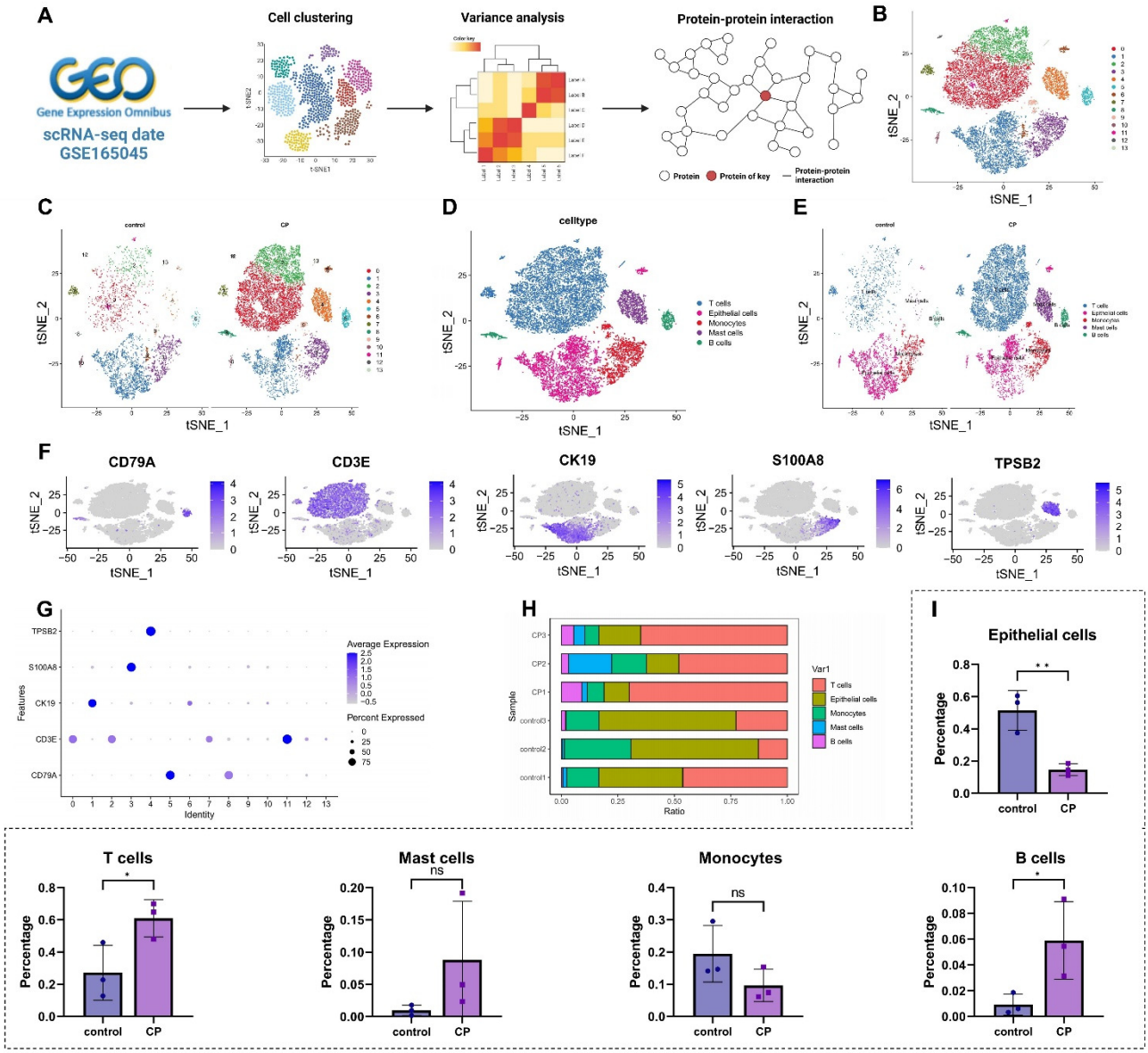

Figure 1. Analysis of scRNA-seq Data.

Note: (A) Simplified workflow for scRNA-seq data analysis; (B) Visualization of TSNE clustering results, showing the aggregation and distribution of cells from different sample sources, with each color representing a distinct cluster; (C) Visualization of TSNE clustering results, illustrating the aggregation and distribution of cells within different groups, where each color indicates a specific cluster; the left image represents the control group, and the right image represents the CP group; (D) Visualization of cell annotation results based on TSNE clustering, with each color representing a different cell subtype; (E) Visualization of cell annotation results based on TSNE clustering, where each color indicates a distinct cell subtype; the left image shows the control group, and the right image shows the CP group; (F) Expression levels of five cell marker genes across various cell subtypes, with darker blue indicating higher average expression levels; (G) Expression patterns of known lineage-specific marker genes across different clusters in control and CP samples, where deeper red indicates higher average expression levels and larger circles represent a greater number of cells expressing that gene; (H) Proportional representation of different cell subtypes in each sample, with subtype types indicated by distinct colors; (I) The *p*-value of the difference in cell content between the control and CP groups was analyzed using a T-test (control, n=3; CP, n=3), with data presented as Mean ± SD. Each group consists of three samples, and * indicates statistical significance (*$p < 0.05$, **$p < 0.01$), while ns denotes no statistical significance.

3.2 T Cells and Nrf2 as Central Players in CP Progression

To further dissect the functional roles of individual cell types, we investigated intercellular communication by analyzing ligand-receptor interactions. Compared to healthy tissue, the CP group demonstrated a global reduction in both the number and strength of cell-cell signaling interactions (Figure

S1A). Interestingly, T cells in CP samples demonstrated enhanced communication activity, while epithelial cells displayed weakened interactions (Figure S1B-C). Pathway-specific analyses further supported these findings: T cells showed increased signaling activity, whereas epithelial cells exhibited diminished pathway engagement (Figure S1D-E). Conclusively, T cells may act as central regulators of intercellular communication in CP, potentially influencing the local inflammatory microenvironment.

To identify molecular drivers of epithelial cell dysfunction in CP, we performed differential gene expression analysis on epithelial cells, uncovering 246 DEGs—169 upregulated and 77 downregulated in CP tissues (Figure 2A).

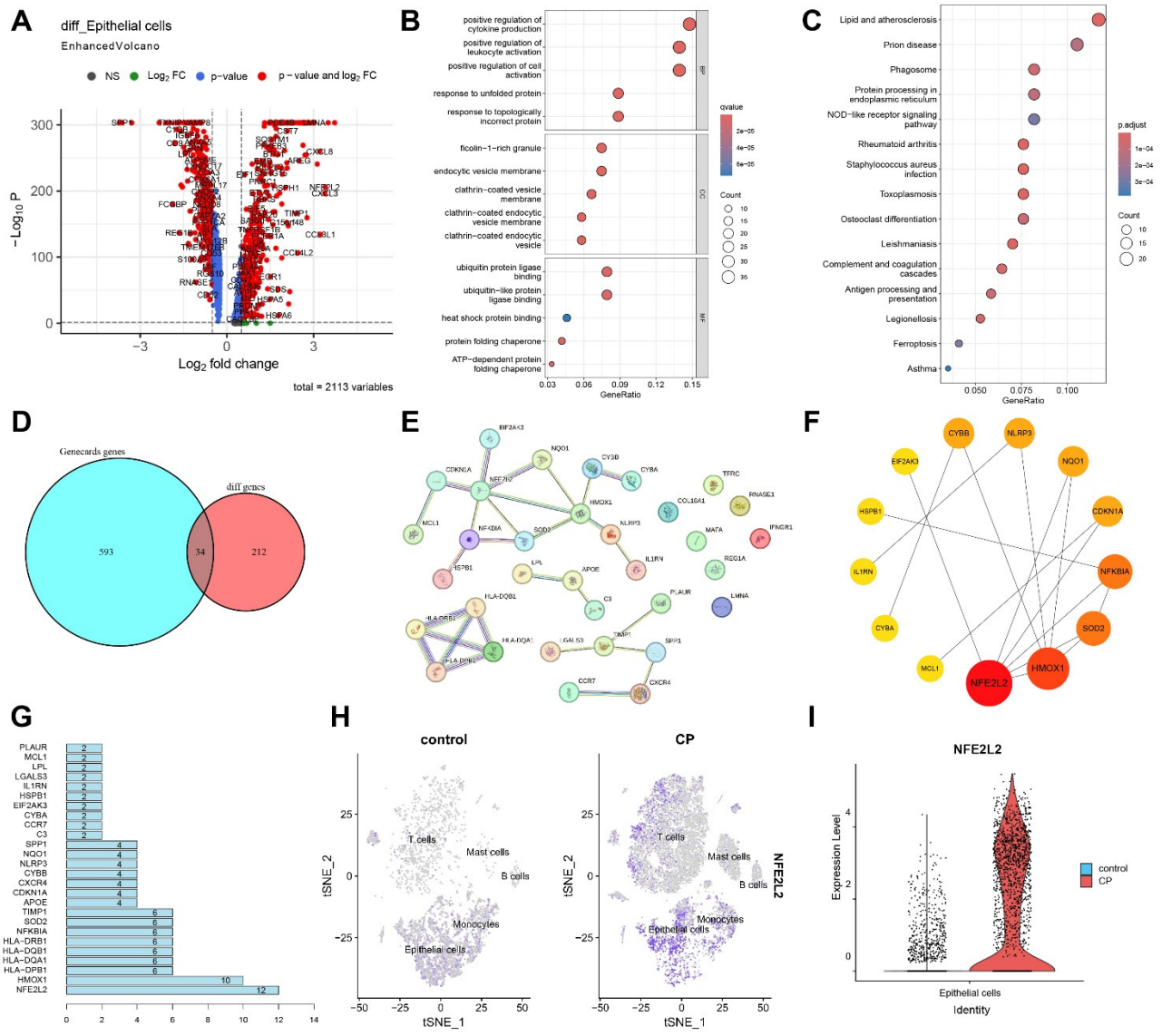

Figure 2. Identification of Key Genes through scRNA-seq Analysis.

Note: (A) Volcano plot of DEGs in epithelial cells from control (n=3) and CP (n=3) groups; red dots to the right of the dashed line represent genes that are downregulated in the CP group, while dots to the left indicate upregulated genes; (B) Bubble plot of GO enrichment analysis for DEGs, where the circle color reflects the level of significance, transitioning from blue to red, and the circle size represents the number of enriched genes; (C) Bubble plot of KEGG enrichment analysis for DEGs, where the circle color indicates significance, with larger circles representing more enriched genes; (D) Venn diagram showing the intersection of DEGs with those in the GeneCard database; (E) PPI network of the 34 intersecting genes (Combined score = 0.7); (F) PPI network of the 34 intersecting genes (Combined score = 0.7), with colors ranging from yellow to red, and circle sizes indicating gene degree from small to large; (G) Statistical analysis of interaction sites within the PPI network for the 34 intersecting genes; (H) Expression levels of the NFE2L2 gene in the scRNA-seq dataset; (I) Expression levels of the NFE2L2 gene in the scRNA-seq dataset.

GO enrichment analysis of these DEGs showed significant involvement in BP such as cytokine production, leukocyte activation, and general immune cell activation. CC terms included ficolin-1-rich granules, endocytic vesicle membranes, and clathrin-coated vesicles. In terms of MF, the DEGs were enriched in ubiquitin protein ligase binding, ubiquitin-like protein ligase binding, and heat shock protein binding (Figure 2B). KEGG pathway analysis revealed that these genes are associated with lipid metabolism, atherosclerosis, prion disease, phagosome formation, protein processing in the endoplasmic reticulum, and the NOD-like receptor signaling pathway. Of particular interest was the enrichment in lipid and atherosclerosis-related genes (Figure 2C).

To identify key disease-associated genes, we obtained 10,714 CP-related genes from the GeneCards database and filtered for those with a relevance score >15, yielding 627 genes. Intersecting these with our DEGs resulted in 34 shared genes (Figure 2D). PPI analysis using the STRING database revealed that *NFE2L2* (also known as Nrf2) was a central hub in the network (Figure 2E-G). Further examination of scRNA-seq data confirmed significantly elevated expression of Nrf2 in CP tissues (Figure 2H), and specifically within epithelial cells (Figure 2I). These results implicate Nrf2 as a potentially critical regulator of immune responses and oxidative stress in the CP microenvironment.

3.3 Silencing Nrf2 Promotes RPDEC Proliferation, Attenuates Inflammation, and Facilitates Anti-Inflammatory T Cell Differentiation

To elucidate the functional role of Nrf2 in RPDECs, we constructed both Nrf2-silenced and Nrf2-overexpressing RPDEC lines. Three shRNA sequences targeting Nrf2 were designed and introduced via lentiviral transduction (Figure S3A). The efficiency of gene modulation was verified through **RT-qPCR** and **WB**. Among the three constructs, *sh-Nrf2-3* (hereafter referred to as *sh-Nrf2*) was the most effective and selected for further analysis (Figure S2).

We then assessed the influence of Nrf2 expression on RPDEC proliferation. CCK-8 and EDU incorporation assays demonstrated that silencing Nrf2 significantly promoted cell viability and proliferation, whereas Nrf2 overexpression led to a notable decline in both parameters (Figure S3B-C). This proliferative effect was further corroborated by increased expression of the proliferation markers Ki67 and PCNA in the sh-Nrf2 group, as determined by WB (Figure S3D).

To simulate an inflammatory environment, we established an *in vitro* pancreatitis model by treating RPDECs with cerulein (Figure S3E). Analysis of apoptosis revealed that Nrf2 silencing markedly reduced apoptosis rates, while Nrf2 overexpression significantly increased cell death (Figure S3F). These findings were confirmed using Hoechst 33342/PI dual staining (Figure S3G). WB further indicated decreased expression of the pro-apoptotic protein Bax and elevated expression of the anti-apoptotic protein Bcl-2 in the sh-Nrf2 group. The opposite pattern was observed in the Nrf2-overexpressing cells (Figure S3H).

We next examined how Nrf2 expression affects cytokine profiles in RPDECs. Notably, silencing Nrf2 suppressed the production of pro-inflammatory cytokines including IL-6, TNF-α, and IL-1β. In contrast,

anti-inflammatory cytokines, such as IL-10 and TGF-β, were upregulated in the sh-Nrf2 group. Nrf2 overexpression led to the reverse cytokine expression pattern (Figure S3I).

Given the increased T cell abundance and interaction strength observed in CP tissues via scRNA-seq, we further explored how Nrf2-modulated RPDECs influence T cell behavior. Co-culture experiments were conducted using T cells and RPDECs from the various experimental groups (Figure S4A). FCM analysis revealed that RPDECs with Nrf2 knockdown significantly reduced the differentiation of T cells into pro-inflammatory Th1 and Tc1 subsets, whereas Nrf2 overexpression promoted this differentiation compared to respective controls (Figure S4B-D). Moreover, the frequency of anti-inflammatory T cell subsets—Th2 and Tc2—was elevated in the sh-Nrf2 group and decreased in the oe-Nrf2 group relative to its respective controls (Figure S4E-G). Correspondingly, the Th1/Th2 and Tc1/Tc2 ratios were notably lower in the sh-Nrf2 group and higher in the oe-Nrf2 group relative to its respective controls (Figure S4H-I).

We also analyzed the abundance of Th17 and Tc17 cells, key drivers of autoimmune and chronic inflammatory responses. The sh-Nrf2 group exhibited a marked reduction in both Th17 and Tc17 cell numbers, whereas these populations were elevated in the oe-Nrf2 group (Figure S4J-L). To determine whether RPDECs influence T cell proliferation, we performed EDU staining on co-cultured T cells. The results showed that RPDECs with silenced Nrf2 inhibited T cell proliferation, while Nrf2-overexpressing RPDECs enhanced it (Figure S4M). These findings suggest that epithelial Nrf2 expression not only modulates inflammatory mediator expression within RPDECs but also affects immune cell behavior through direct or paracrine signaling.

Collectively, our findings demonstrate that Nrf2 silencing in RPDECs enhances cell proliferation, reduces apoptosis, and shifts cytokine expression toward an anti-inflammatory profile. Additionally, these changes in epithelial cells significantly influence T cell differentiation by promoting anti-inflammatory subsets and inhibiting pro-inflammatory ones, along with reducing T cell proliferation. This suggests a central role for epithelial Nrf2 in regulating immune responses and epithelial regeneration in the context of CP.

3.4 Silencing Nrf2 Alleviates Inflammation and Fibrosis in a Rat Model of CP

To investigate the *in vivo* role of Nrf2 in the progression of CP, we established rat models with either Nrf2 knockdown or overexpression by injecting lentiviral constructs. CP was induced in all animals via DBTC administration over two consecutive weeks (Figure S5A).

H&E staining of pancreatic tissue revealed typical pathological features of CP in both control groups (sh-NC and oe-NC), including parenchymal necrosis, fat necrosis, inflammatory infiltration, acinar cell lysis, and marked cellular depletion. These tissues also displayed severe edema, sublobular hemorrhage, and neutrophil infiltration. In contrast, Nrf2 silencing alleviated these pathological changes, whereas Nrf2 overexpression intensified tissue injury (Figure S5B). Histopathological scoring supported these observations (Figure S5C). Additionally, the volume of ascitic fluid was significantly reduced in the sh-Nrf2 group compared to sh-NC, whereas rats in the oe-Nrf2 group exhibited increased ascites relative to the oe-NC group (Figure S5D).

We further assessed CP-related biochemical indices, including serum AMY (Figure S5E), serum lipase (Figure S5F), pancreatic trypsin activity (Figure S5G), pancreatic neutrophil recruitment (determined by MPO activity, Figure S5H), and pancreatic necrosis (indicated by HMGB1 levels, Figure S5I). These markers were all notably diminished in the Nrf2-silenced group and elevated in the Nrf2-overexpressing group, suggesting that Nrf2 knockdown mitigates pancreatic injury, whereas its overexpression exacerbates it. To evaluate systemic inflammation, we measured serum concentrations of key cytokines. Nrf2 silencing significantly downregulated pro-inflammatory cytokines—IL-6, TNF-α, and IL-1β—while elevating anti-inflammatory cytokines IL-10 and TGF-β. Conversely, Nrf2 overexpression led to elevated levels of IL-6, TNF-α, and IL-1β and reduced levels of IL-10 and TGF-β (Figure S5J-N). These results further highlight the pro-inflammatory role of Nrf2 in CP progression.

To investigate the extent of pancreatic fibrosis, we performed Masson's trichrome staining and Sirius Red staining on pancreatic sections. Nrf2 overexpression resulted in pronounced perivascular collagen deposition, while its silencing markedly reduced fibrotic staining (Figure S6A-B). TUNEL assays showed reduced apoptotic cell numbers in the sh-Nrf2 group and increased apoptosis in the oe-Nrf2 group (Figure S6C). Immunofluorescence staining further revealed that expression of α-SMA, a marker of activated pancreatic stellate cells and fibrosis, was decreased in Nrf2-silenced animals and elevated in those overexpressing Nrf2 (Figure S6D).

At the transcriptional level, we measured mRNA expression of several key fibrosis-related genes, including α-SMA, collagen type I alpha 1 (Col1a1), connective tissue growth factor (CTGF), and fibronectin-1 (FN1). All four genes were distinctly downregulated in the sh-Nrf2 group, whereas their expression was markedly upregulated in the oe-Nrf2 group (Figure S6E-H), indicating a profibrotic role for Nrf2 in CP.

Overall, our *in vivo* findings demonstrate that silencing Nrf2 alleviates pancreatic inflammation and fibrosis in DBTC-induced CP rats. This protective effect is evidenced by reduced tissue injury, diminished inflammatory cytokine expression, decreased fibrosis markers, and lower apoptosis rates.

3.5 Silencing Nrf2 Mitigates Immune Cell Infiltration and Promotes Anti-Inflammatory T Cell Differentiation in CP Rats

To further elucidate the immunomodulatory role of Nrf2 *in vivo*, we assessed its protein expression in the pancreatic tissue of CP rats using immunofluorescence staining. The results demonstrated that Nrf2 expression was evidently downregulated in the sh-Nrf2 group, whereas Nrf2 was markedly upregulated in the oe-Nrf2 group (Figure 3A). We next examined immune cell infiltration using immunohistochemical staining for cellular markers. The results demonstrated that the pancreatic tissues of Nrf2-silenced rats exhibited a reduction in infiltrating lymphocytes (CD3), neutrophils (CD11b), and macrophages (F4/80). In contrast, overexpression of Nrf2 resulted in a significant increase in all three immune cell types (Figure 3B). These findings were further supported by mRNA analysis: expression of CD11b, CD3e (T cell marker), and mannose receptor C-type 1 (Mrc1), a macrophage marker, was decreased in the sh-Nrf2 group and elevated in

the oe-Nrf2 group (Figure 3C). Collectively, these data indicate that Nrf2 silencing suppresses immune cell infiltration, while its overexpression promotes immune cell recruitment to pancreatic tissue.

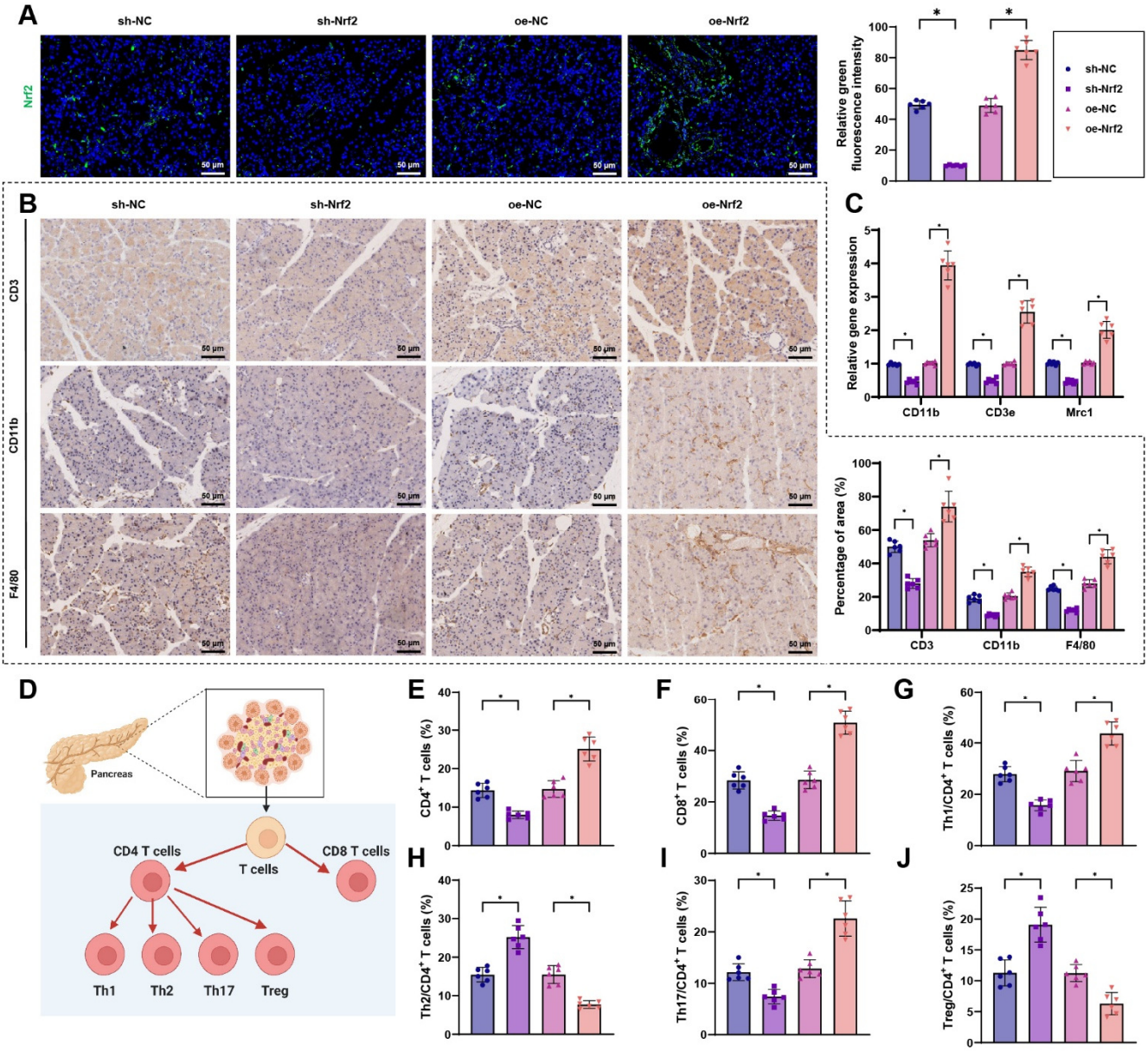

Figure 3. Effects of Nrf2 on Immune Infiltration and T Cell Differentiation in CP Rats.
Note: (A) Immunofluorescence staining showing the expression of the Nrf2 gene in pancreatic tissues of different intervention groups; (B) Immunohistochemical analysis of CD3, CD11b, and F4/80 protein expression in pancreatic tissues of different intervention groups (scale bar = 50 μm, n = 6); (C) RT-qPCR analysis of CD11b, CD3e, and Mrc1 expression in pancreatic tissues of different intervention groups; (D) Schematic representation of T cell subtypes in pancreatic tissue; (E-J) Statistical analysis of $CD4^+$ T cells, $CD8^+$ T cells, Th1, Th2, Th17, and Treg cell counts in pancreatic tissue. Measurement data are presented as Mean ± SD, data were analyzed using one-way ANOVA, with six rats in each group, n=6. * indicates comparisons between two groups, *$p < 0.05$.

To evaluate how Nrf2 affects T cell differentiation in vivo, we performed FCM analysis on pancreatic tissues (Figure 3D). Silencing Nrf2 significantly reduced the proportions of both $CD4^+$ and $CD8^+$ T cells, while overexpression of Nrf2 led to opposite trends (Figure 3E-F). Furthermore, the sh-Nrf2 group exhibited a reduced frequency of pro-inflammatory Th1 and Th17 cells, while Th2 and Tregs were markedly increased. Conversely, Nrf2 overexpression favored the expansion of Th1 and Th17 cells and suppressed Th2 and Treg differentiation (Figure 3G-J).

These findings suggest that Nrf2 knockdown favors a shift toward anti-inflammatory T cell phenotypes and reduces T cell-driven immune responses within the pancreas.

3.6 BA Promotes RPDEC Proliferation and Promotes Anti-Inflammatory T Cell Polarization

BA (Figure S7A), a flavonoid compound derived from *Scutellaria baicalensis*, is known for its potent anti-inflammatory and antioxidant properties. Previous studies have demonstrated that BA confers protection in acute pancreatitis by reducing inflammation and oxidative damage [33-35]. However, limited evidence is available regarding its function in CP.

To assess the impact of BA on CP, an in vitro RPDEC injury model was established using cerulein stimulation, followed by treatment with increasing concentrations of BA (Figure S7B). EDU incorporation assays showed that cerulein exposure significantly suppressed RPDEC proliferation, while BA treatment restored cell proliferation in a dose-dependent fashion (Figure S7C). Hoechst 33342/PI double staining and FCM further confirmed that BA reduced apoptosis of cerulein-injured RPDECs, with higher BA concentrations exerting stronger anti-apoptotic effects (Figure S7D-E).

WB analysis supported these observations: expression of Ki67, PCNA, and Bcl-2—markers of cell proliferation and survival—was suppressed by cerulein but upregulated following BA treatment in a concentration-dependent fashion. In contrast, the pro-apoptotic protein Bax was elevated in cerulein-treated cells and suppressed by BA. These data indicate that BA enhances epithelial regeneration and protects RPDECs against injury-induced apoptosis (Figure S7F).

To further explore the immunomodulatory effects of BA, we co-cultured BA-treated RPDECs with T cells and assessed T cell polarization. FCM analysis showed that BA significantly suppressed the differentiation of T cells into Th1 and Tc1 subsets (Figure 4A-C), while promoting their differentiation into Th2 and Tc2 cells (Figure 4D-F). Consequently, the Th1/Th2 and Tc1/Tc2 ratios were distinctly declined in a BA concentration-dependent fashion (Figure 4G-H). Additionally, BA inhibited the differentiation of Th17 and Tc17 subsets (Figure 4I-K). EDU assays showed that BA also dose-dependently reduced T cell proliferation (Figure 4L), suggesting that BA not only alters T cell fate but also restrains their expansion.

Taken together, our findings indicate that silencing Nrf2 in CP rats alleviates immune cell infiltration and reprograms T cell responses toward anti-inflammatory phenotypes, thereby reducing local inflammatory activity. In parallel, BA enhances RPDEC proliferation, inhibits apoptosis, and suppresses T cell-driven inflammation by promoting anti-inflammatory T cell differentiation and limiting T cell proliferation.

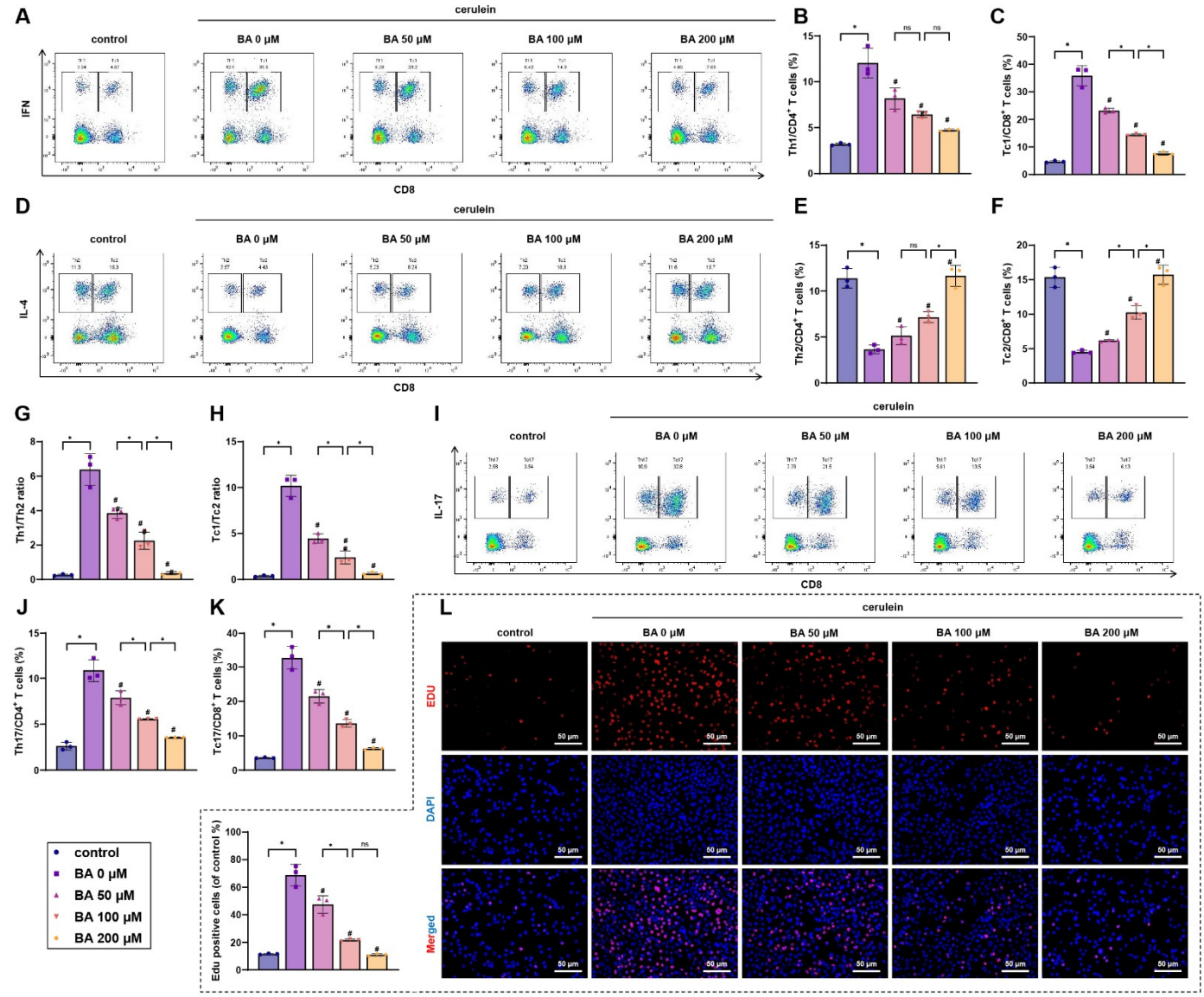

Figure 4. Effects of BA on T Cell Differentiation.

Note: (A-C) FCM analysis of Th1 and Tc1 cell counts in different treatment groups; (D-F) FCM analysis of Th2 and Tc2 cell counts in different treatment groups; (G) Ratio of Th1 to Th2 cell counts in different treatment groups; (H) Ratio of Tc1 to Tc2 cell counts in different treatment groups; (I-K) FCM analysis of Th17 and Tc17 cell counts in different treatment groups; (L) EDU assay assessing T cell proliferation in different treatment groups, with EDU-positive cells shown in red (indicating the proliferative phase), and blue representing DAPI-stained cell nuclei (scale bar = 25 μm). Data are presented as Mean ± SD, data were analyzed using one-way ANOVA, with each experiment repeated three times, n=3. * indicates significance between groups, *$p < 0.05$. # indicates significance compared to the BA 0 μM group, #$p < 0.05$.

3.7 BA Alleviates CP Symptoms by Inhibiting Inflammation and Fibrosis in Rats

To evaluate the *in vivo* therapeutic potential of BA in CP, we induced CP in rats using DBTC and administered BA at varying concentrations via tail vein injection (Figure 5A).

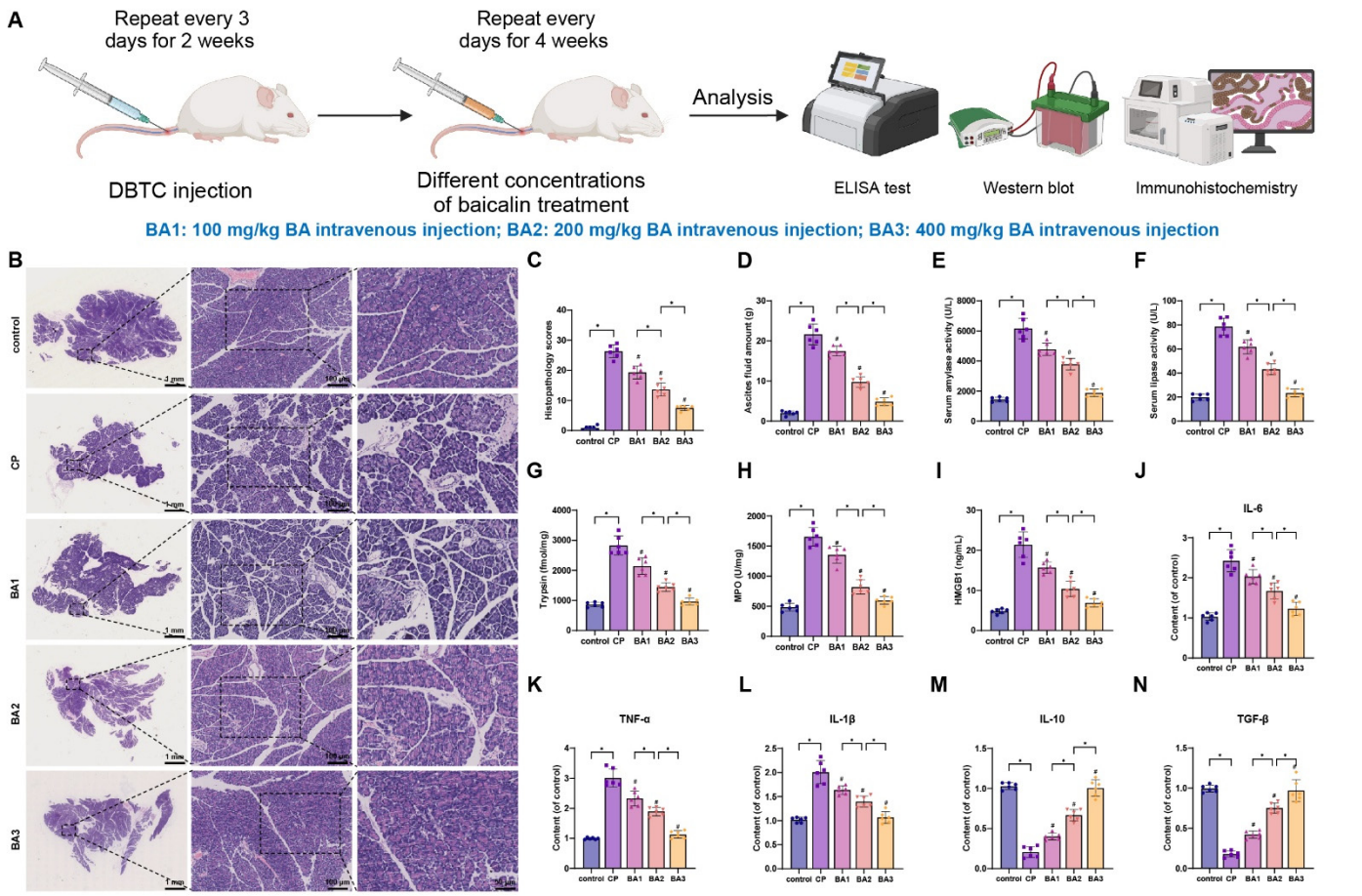

Figure 5. BA Ameliorates Symptoms of CP in the CP Rat Model.

Note: (A) Schematic diagram of the experimental procedure for BA treatment in CP rats; (B) H&E staining showing changes in pancreatic tissue structure (scale bar = 1 mm/100 μm/50 μm, n = 6); (C) Histopathological scoring of pancreatic tissue in rats (n = 6); (D) Measurement of ascites volume in rats (n = 6); (E) Serum AMY activity assay in rats (n = 6); (F) Serum lipase activity assay in rats (n = 6); (G) Pancreatic protease activity assay in rats (n = 6); (H) Pancreatic MPO activity assay in rats (n = 6); (I) Detection of HMGB1 levels in pancreatic tissue from rats (n = 6); (J-N) ELISA assessment of serum levels of IL-6, TNF-α, IL-1β, IL-10, and TGF-β in rats (n = 6). Data are expressed as mean ± SD, data were analyzed using one-way ANOVA, with each group consisting of six rats. n=6. * indicates comparison between two groups, *$p < 0.05$. # denotes comparison with the CP group, #$p < 0.05$.

In the control group, pancreatic tissue maintained a normal acinar structure. In contrast, the CP group displayed hallmark pathological changes, including extensive parenchymal and fat necrosis, inflammatory cell infiltration, cell lysis, and a substantial reduction in acinar cell number. Additionally, there was pronounced edema, sublobular hemorrhage, and neutrophil infiltration, all contributing to elevated histopathological scores and increased ascitic fluid volume. Treatment with BA markedly attenuated pancreatic injury, reduced pathological scores, and decreased ascites accumulation. These effects were dose-dependent, with higher BA concentrations producing more significant improvements (Figure 5B-D).

We next assessed several biochemical markers associated with pancreatic injury. BA treatment significantly decreased levels of serum AMY (Figure 5E), serum lipase (Figure 5F), pancreatic trypsin activity (Figure 5G), and MPO activity—a marker of neutrophil recruitment (Figure 5H). Furthermore, pancreatic necrosis, indicated by HMGB1 levels, was also mitigated by BA treatment (Figure 5I). We also analyzed systemic inflammatory responses by measuring serum levels of key cytokines. BA administration suppressed

the expression of IL-6, TNF-α, and IL-1β, while simultaneously enhancing the levels of IL-10 and TGF-β. These immunomodulatory effects were more pronounced at higher BA concentrations (Figure 5J-N).

Masson's trichrome and Sirius Red staining analyses demonstrated that BA significantly reduced perivascular collagen deposition and mitigated fibrotic remodeling in the pancreas (Figure S8A-B). TUNEL staining further showed that BA treatment reduced apoptosis in pancreatic tissue in a dose-dependent fashion (Figure S8C). Consistently, immunofluorescence analysis indicated a notable reduction in α-SMA following BA administration (Figure S8D). At the molecular level, BA also downregulated the expression of α-SMA, Col1a1, CTGF, and FN1. These mRNA levels decreased significantly with increasing BA concentrations (Figure S8E-H), further confirming BA's anti-fibrotic potential.

In summary, BA treatment significantly improved CP symptoms and inhibited pancreatic fibrosis in CP rats.

3.8 BA Reduces Immune Infiltration in Pancreatic Tissue and Promotes Anti-inflammatory T Cell Differentiation in CP Rats

To examine the immunomodulatory effects of BA on CP, we analyzed immune cell infiltration within pancreatic tissues using immunohistochemical staining. Compared to healthy controls, pancreatic tissues from CP rats exhibited substantial increases in lymphocytes ($CD3^+$), neutrophils ($CD11b^+$), and macrophages ($F4/80^+$), indicating a heightened immune response. Notably, BA treatment led to a dose-dependent reduction in all three immune cell types (Figure 6A-D). These histological findings were supported at the transcriptional level. qPCR analysis revealed significantly elevated mRNA expression of CD11b, CD3e, and Mrc1 in CP tissues, all of which were gradually downregulated following BA treatment, in proportion to increasing BA concentrations (Figure 6E-G). These data suggest that BA effectively suppresses immune cell infiltration in the pancreas during CP.

To assess the impact of BA on T cell composition and differentiation, we performed FCM on pancreatic tissue samples. The results demonstrated a significant elevation in $CD4^+$ and $CD8^+$ T cell populations in the CP group compared to controls. However, these populations were markedly reduced following BA administration (Figure 6H-I). Further analysis of T cell subsets revealed that BA treatment inhibited the differentiation of T cells into pro-inflammatory phenotypes, specifically Th1 and Th17 cells, while simultaneously promoting their differentiation into anti-inflammatory subsets, including Th2 and Treg cells. These regulatory shifts became more pronounced at higher BA doses (Figure 6J-M). The findings clearly indicate that BA modulates T cell polarization toward an anti-inflammatory phenotype, thereby dampening T cell–mediated immune responses.

Collectively, these results demonstrate that BA treatment reduces immune cell infiltration and modulates T cell differentiation in favor of anti-inflammatory phenotypes in a CP rat model. By inhibiting pro-inflammatory T cell subtypes and enhancing regulatory populations, BA contributes to the attenuation of immune-driven inflammation in pancreatic tissue.

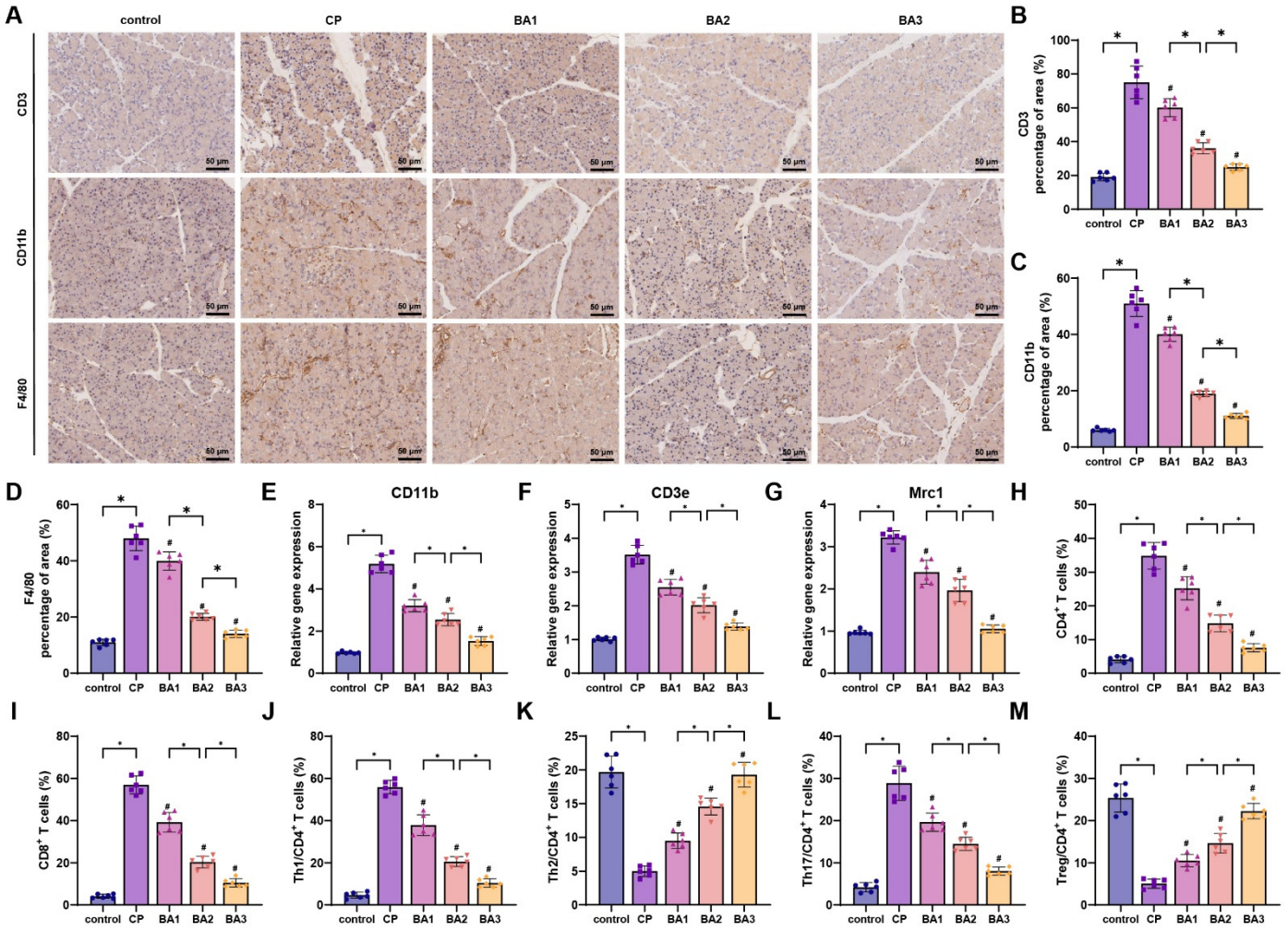

Figure 6. Effects of BA on Immune Infiltration and T Cell Differentiation in CP Rats.
Note: (A) Immunohistochemical analysis of CD3, CD11b, and F4/80 protein expression in rat pancreatic tissue (scale bar = 50 μm, n = 6); (B-D) Statistical results of histological assessments from immunohistochemical staining (n = 6); (E-G) RT-qPCR analysis of CD11b, CD3e, and Mrc1 expression levels in rat pancreatic tissue (n = 6); (H-M) FCM analysis of $CD4^+$ T cells, $CD8^+$ T cells, Th1, Th2, Th17, and Treg cell counts in pancreatic tissue (n = 6). Data are presented as Mean ± SD, data were analyzed using one-way ANOVA, with each group comprising six rats, n=6. Statistical significance is indicated by * for comparisons between two groups (*$p < 0.05$) and # for comparisons with the CP group (#$p < 0.05$).

3.9 Multi-Omics Sequencing Reveals that BA Suppresses the JAK-STAT Signaling Pathway by Upregulating SIRT5

To elucidate the molecular mechanisms concerning the therapeutic significance of BA in CP, we conducted bulk RNA sequencing (bulk RNA-seq) on pancreatic tissues from the CP group and the BA3 group (Figure 7A). A total of 1,552 DEGs were identified, comprising 1,184 upregulated and 368 downregulated genes in the BA3 group compared to CP (Figure 7B).

GO enrichment analysis of DEGs revealed that the most prominent BP included actin filament organization, regulation of actin-based processes, and cytokine-mediated signaling. In terms of CC, DEGs were enriched in the actin cytoskeleton, membrane rafts, and microdomains. For MF, notable enrichments included cytokine receptor binding, actin binding, and actin filament binding (Figure 7C). KEGG pathway analysis identified key pathways associated with the DEGs, including the JAK-STAT signaling, Salmonella infection, Hepatitis B, lipid and atherosclerosis, and apoptosis. Of particular interest, numerous genes were

enriched in the JAK-STAT signaling pathway (Figure 7D). As shown in Figure S9, WB confirmed that expression of the JAK-STAT pathway-related proteins was reduced in the BA3 group compared to CP, indicating suppression of this pathway.

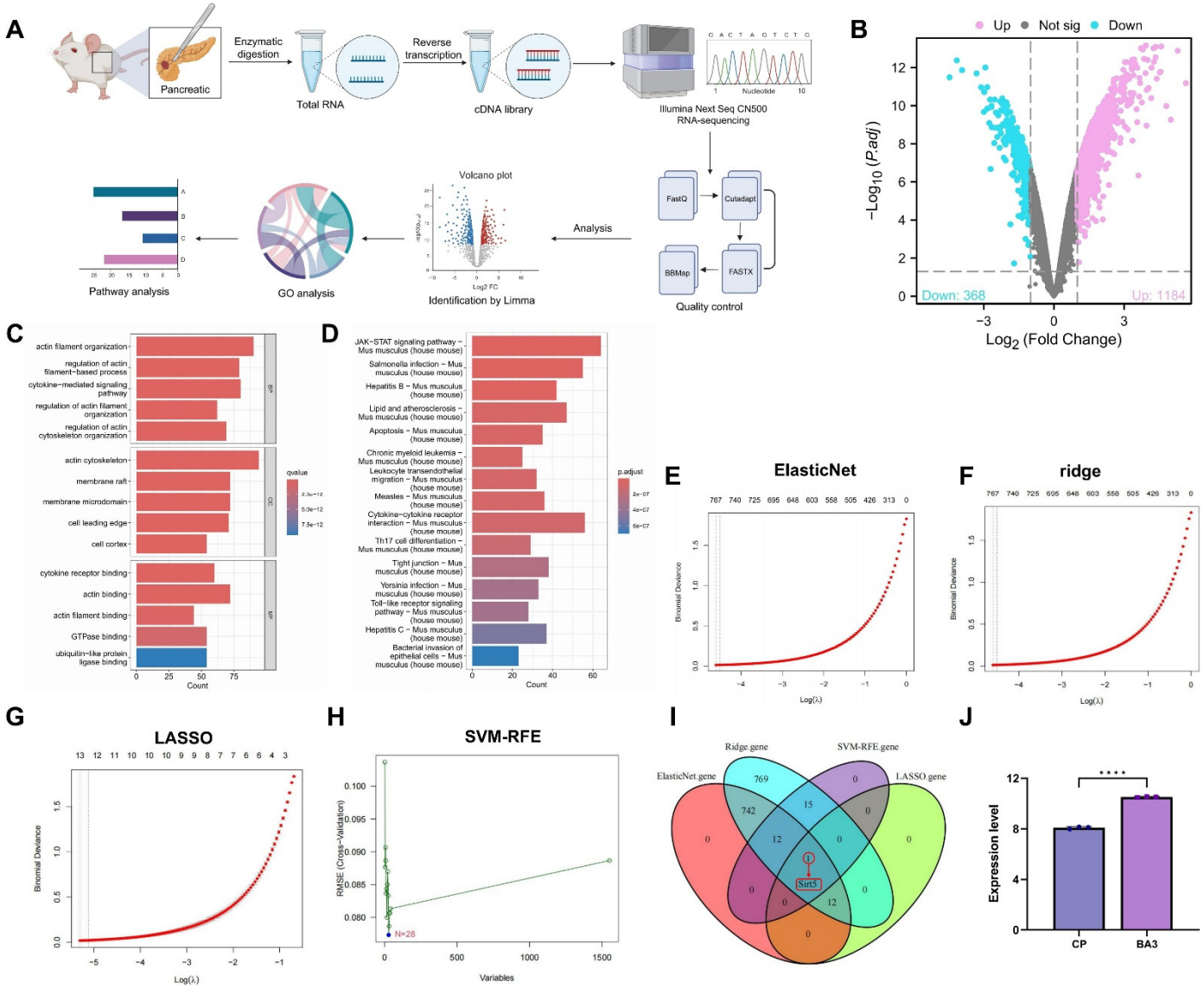

Figure 7. Analysis of Bulk RNA-seq Data to Identify Key Genes.

Note: (A) Schematic diagram of the high-throughput transcriptomic sequencing analysis workflow; (B) Volcano plot of DEGs in pancreatic tissue samples from three CP and three BA3 group rats, with pink indicating upregulated genes, blue indicating downregulated genes, and gray indicating non-DEGs; (C) Bar chart of GO enrichment analysis for DEGs from Bulk RNA-seq, where color intensity from blue to red indicates the degree of significance, and bar length represents the number of enriched genes; (D) Bar chart of KEGG enrichment analysis for DEGs from Bulk RNA-seq, with color intensity indicating significance and bar length representing the number of enriched genes; (E) Selection of 767 feature genes using the ElasticNet algorithm; (F) Selection of 767 feature genes using the ridge regression algorithm; (G) Selection of 13 feature genes using the LASSO algorithm; (H) Selection of 28 feature genes using the SVM-RFE algorithm; (I) Venn diagram of gene intersections identified by four machine learning algorithms; (J) Expression levels of Sirt5 in the Bulk RNA-seq data. Quantitative data are expressed as Mean ± SD, data were analyzed using t-test, and all experiments were conducted in triplicate. * indicates a comparison between two groups with ****$p < 0.0001$.

To further pinpoint genes associated with BA's therapeutic effects, we applied four machine learning algorithms to the DEGs: ElasticNet, ridge regression, LASSO regression, and SVM-RFE. Both ElasticNet and ridge regression identified 767 genes (Figure 7E-F), while LASSO regression, using cross-validation and minimal error criteria, identified 13 genes (Figure 7G). The SVM-RFE algorithm, using the "svmRadial"

method, yielded 28 candidate genes (Figure 7H). Intersecting the results from all four models, SIRT5 emerged as the sole overlapping gene (Figure 7I). Bulk RNA-seq expression data showed that SIRT5 was significantly upregulated in BA-treated tissues (Figure 7J), implicating it as a potential mediator of BA's protective effects in CP.

To validate transcriptomic findings at the protein level, we performed label-free quantitative proteomic analysis on pancreatic tissues from the CP and BA3 groups (Figure S10A). PCA and PLS-DA showed clear separation between the groups, indicating robust differences in protein expression profiles (Figure S10B-C). Additionally, we identified 120 differentially expressed proteins—72 upregulated and 48 downregulated in BA-treated samples (Figure S10D).

GO and KEGG enrichment analyses indicated that these proteins were mainly involved in reactive oxygen species (ROS) metabolism, collagen-containing extracellular matrix, glycosaminoglycan binding, and the JAK-STAT signaling in Mus musculus (house mouse) (Figure S10E-F). Notably, KEGG also revealed significant enrichment in the Th17 cell differentiation pathway, supporting a role for BA in immune regulation via T cell modulation.

PPI network analysis using the STRING database identified central hub proteins within the JAK-STAT pathway, underscoring their functional importance (Figure S10G). Furthermore, SIRT5 protein expression was elevated in the BA3 group, while JAK-STAT pathway proteins were suppressed (Figure S10H), confirming the transcriptomic findings.

In conclusion, combined transcriptomic and proteomic analyses reveal that BA treatment upregulates SIRT5 expression and inhibits the JAK-STAT pathway in the pancreatic tissue of CP rats.

3.10 BA Ameliorates CP via SIRT5-Mediated Nrf2 Deacetylation and Suppression of the JAK-STAT Axis

Sirtuins (SIRT1-7) are a class of NAD^+-dependent histone deacetylases involved in regulating redox balance, oxidative stress, and immune responses. Among them, SIRT5 has been shown to regulate Nrf2 by modulating its acetylation status, thereby influencing Nrf2's stability, nuclear localization, and transcriptional activity [36-38]. Based on our multi-omics sequencing results, we hypothesized that BA alleviates CP by upregulating SIRT5, which promotes Nrf2 deacetylation, ultimately leading to inhibition of the JAK-STAT pathway and suppression of inflammation.

To validate this mechanism, we examined acetylated Nrf2 (Ac-Nrf2) levels in pancreatic tissue by WB. The results showed a dose-dependent reduction in Ac-Nrf2 following BA treatment (Figure 8A). Confocal microscopy further demonstrated a progressive decrease in Nrf2 nuclear fluorescence intensity with increasing BA concentrations (Figure 8B), consistent with reduced Nrf2 activity under increased deacetylation. Next, we measured the expression of SIRT5, Janus kinase 1 (JAK1), and Signal transducer and activator of transcription 3 (STAT3) in pancreatic tissues from each group. Compared to controls, the CP group showed downregulation of SIRT5 and upregulation of JAK1 and STAT3. BA treatment reversed these trends, with SIRT5 expression increasing and JAK1/STAT3 levels decreasing in a concentration-dependent fashion (Figure 8C). Notably, phosphorylated JAK2 (p-JAK2) and phosphorylated STAT3 (p-STAT3) were

significantly elevated in CP, indicating pathway activation, whereas BA markedly suppressed their phosphorylation (Figure 8D). These results collectively indicate that BA suppresses the JAK-STAT signaling cascade by enhancing SIRT5-mediated deacetylation of Nrf2.

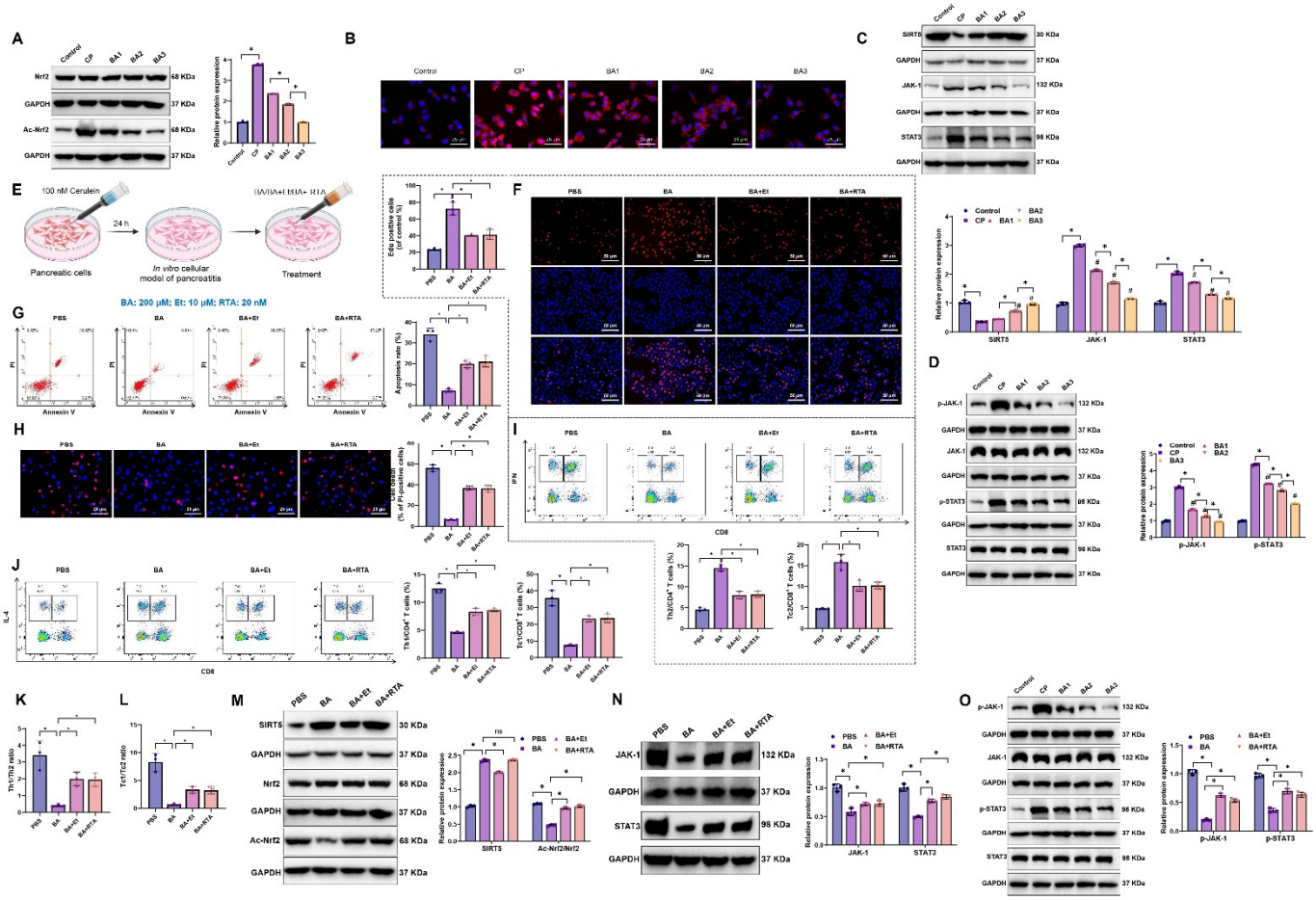

Figure 8. BA Improves CP by SIRT5-Mediated Deacetylation of Nrf2 and Inhibition of the JAK/STAT Pathway. Note: (A) WB analysis showing changes in Nrf2 and Ac-Nrf2 protein expression in rat pancreatic tissue (n=6); (B) Immunofluorescence analysis of Nrf2 localization and expression in RPDECs from different treatment groups. Red: Nrf2 protein; Blue: DAPI-stained nuclei (scale bar = 25 μm); (C) WB analysis showing changes in SIRT5, JAK1, and STAT3 protein expression in rat pancreatic tissue (n=6); (D) WB analysis of phosphorylated JAK1 and STAT3 (p-JAK1 and p-STAT3) protein levels in rat pancreatic tissues (n = 6); (E) Schematic diagram of the cell experiment workflow; (F) EDU assay demonstrating the proliferation ability of RPDECs in different treatment groups, with red indicating EDU-positive cells in the proliferative phase and blue indicating DAPI-stained cell nuclei (scale bar=50 μm); (G) Annexin V/PI double staining followed by FCM to assess apoptosis in RPDECs from different treatment groups, with the bar graph representing the proportion of apoptotic cells in Q2 and Q3 quadrants; (H) Hoechst 33342/PI double staining assessing apoptosis/necrosis in RPDECs from different treatment groups, with red indicating apoptotic or necrotic cells and blue indicating healthy cells (scale bar=25 μm); (I) FCM analysis of Th1 and Tc1 cell numbers in different treatment groups; (J) FCM analysis of Th2 and Tc2 cell numbers in different treatment groups; (K) Ratio of Th1 to Th2 cell numbers in different treatment groups; (L) Ratio of Tc1 to Tc2 cell numbers in different treatment groups; (M) WB analysis of SIRT5, Nrf2, and Ac-Nrf2 protein expression changes in RPDECs from different treatment groups; (N) WB analysis of JAK1 and STAT3 protein expression changes in RPDECs from different treatment groups. Data are presented as Mean ± SD, with each experiment repeated three times; (O) WB analysis of phosphorylated JAK1 and STAT3 (p-JAK1 and p-STAT3) protein levels in RPDECs (n = 6). Quantitative data are presented as Mean ± SD. Cell-based experiments: n = 3; animal experiments: n = 6. Statistical analysis was performed using one-way ANOVA. * indicates a significant difference between two groups, *p<0.05. Et-29: SIRT5 inhibitor; RTA-408: Nrf2 activator.

To further explore the functional role of SIRT5 and Nrf2 in mediating BA's effects, we established an *in vitro* cerulein-induced pancreatitis model using RPDECs. Cells were treated with BA, either alone or in combination with the SIRT5 inhibitor Et-29 (Et) or the Nrf2 activator RTA-408 (RTA) (Figure 8E). EDU

assays showed that BA treatment significantly promoted RPDEC proliferation, whereas co-treatment with Et or RTA partially reversed this proliferative effect (Figure 8F). Apoptosis analysis via FCM and Hoechst 33342/PI staining revealed that BA reduced apoptosis, while Et or RTA restored apoptotic levels (Figure 8G-H).

To evaluate immune-modulating effects, BA-treated RPDECs were co-cultured with T cells. FCM analysis revealed that BA inhibited Th1 and Tc1 differentiation (Figure 8I) and enhanced Th2 and Tc2 differentiation (Figure 8J). These effects resulted in significantly lower Th1/Th2 and Tc1/Tc2 ratios (Figures 8K-L), further supporting a regulatory role for BA in immune balance. Importantly, the co-administration of Et or RTA reversed the effects of BA on T cell polarization, confirming the involvement of the SIRT5-Nrf2 axis. We next confirmed the molecular changes underlying the observed phenotypes. BA treatment led to a notable elevation in total SIRT5 expression and a reduction in Ac-Nrf2 protein levels, indicating enhanced Nrf2 deacetylation. Et treatment suppressed SIRT5 expression and restored Ac-Nrf2 levels, suggesting that BA's effect on Nrf2 acetylation is SIRT5-dependent. Additionally, total Nrf2 protein levels were increased by BA (Figure 8M). Moreover, BA suppressed JAK1 and STAT3 protein expression, an effect reversed by Et or RTA co-treatment (Figure 8N). This was accompanied by reduced levels of p-JAK2 and p-STAT3 in the BA group, with re-elevation of these phosphorylated forms upon SIRT5 inhibition or Nrf2 activation (Figure 8O).

To further validate the hypothesis that BA improves CP symptoms through SIRT5-mediated deacetylation of Nrf2, we established a DBTC-induced CP rat model and administered treatments via tail vein injection. Rats were divided into groups receiving BA alone, BA in combination with Et, or BA combined with RTA (Figure S11A). In the PBS group, pancreatic tissues exhibited classic pathological features including extensive fat and parenchymal necrosis, inflammatory cell infiltration, acinar lysis, and reduced cell density, resulting in elevated histopathological scores and increased ascites. BA administration significantly ameliorated these histological abnormalities, reduced ascitic fluid accumulation, and improved tissue integrity. However, the therapeutic benefits of BA were substantially attenuated when co-administered with either Et or RTA (Figure S11B-D).

Key biochemical markers associated with pancreatic injury were evaluated. BA significantly reduced serum AMY (Figure S11E), serum lipase (Figure S11F), pancreatic trypsin activity (Figure S11G), neutrophil infiltration in the pancreas (Figure S11H), and pancreatic necrosis (Figure S11I). These improvements were negated when BA was combined with Et or RTA. Cytokine profiling revealed that BA suppressed the expression of IL-6, TNF-α, and IL-1β, while enhancing the levels of IL-10 and TGF-β. These beneficial immunomodulatory effects were reversed by Et or RTA treatment (Figure S11J-N).

Histological evaluation using Masson's trichrome and Sirius Red staining demonstrated that BA treatment significantly reduced collagen deposition and perivascular fibrosis. In contrast, the co-administration of Et or RTA exacerbated fibrotic changes (Figure S12A-B). TUNEL assays showed that BA attenuated acinar cell apoptosis, whereas Et and RTA restored apoptotic levels (Figure S12C).

Immunofluorescence staining revealed a marked decrease in α-SMA expression following BA treatment (Figure S12D), with consistent findings at the mRNA level for α-SMA, Col1a1, CTGF, and fibronectin-1, all of which were significantly downregulated by BA and upregulated upon co-treatment with Et or RTA (Figure S12E-H).

Immunohistochemical analysis showed that BA substantially decreased the infiltration of lymphocytes ($CD3^+$), neutrophils ($CD11b^+$), and macrophages ($F4/80^+$) in pancreatic tissues. These effects were reversed by co-treatment with Et or RTA (Figure S13A). Similarly, the mRNA expression levels of CD11b, CD3e, and Mrc1 were downregulated by BA and re-elevated upon Et or RTA administration (Figure S13B), indicating that BA suppresses immune cell infiltration in a SIRT5/Nrf2-dependent manner.

FCM revealed that BA significantly reduced $CD4^+$ and $CD8^+$ T cell populations in CP pancreatic tissues. In contrast, Et or RTA co-treatment restored T cell abundance (Figure S13C-D). Furthermore, BA treatment inhibited the differentiation of Th1 and Th17 cells while promoting the generation of Th2 and Treg cells. These effects were also abrogated by Et or RTA (Figure S13E-H), supporting the immunoregulatory role of the SIRT5-Nrf2-JAK/STAT axis.

Mechanistically, BA treatment significantly upregulated SIRT5 protein levels and downregulated Ac-Nrf2, indicating enhanced Nrf2 deacetylation. Et co-treatment reduced SIRT5 expression and increased Ac-Nrf2 levels, further confirming the dependency on SIRT5. Additionally, total Nrf2 protein expression was increased following BA administration (Figure S13I). Importantly, BA suppressed JAK1 and STAT3 protein expression, which was reversed by Et or RTA (Figure S13J). Moreover, levels of p-JAK2 and p-STAT3 were notably lower in BA-treated rats and restored upon Et or RTA co-treatment, indicating reactivation of the JAK-STAT pathway when the SIRT5-Nrf2 regulatory axis is disrupted.

In summary, these *in vivo* findings demonstrate that BA exerts protective effects against CP by upregulating SIRT5, promoting Nrf2 deacetylation, and suppressing the JAK-STAT pathway. This cascade leads to enhanced epithelial regeneration, reduced inflammation and fibrosis, and reprogramming of T cells toward anti-inflammatory phenotypes.

4. Discussion

This study comprehensively elucidates the therapeutic mechanisms of **BA** in **CP** by integrating *in vivo*, *in vitro*, and multi-omics bioinformatics analyses. Our findings reveal that BA exerts protective effects in CP by modulating the **acetylation status of Nrf2** through **SIRT5**, thereby attenuating immune infiltration and fibrotic remodeling within the pancreas. CP is a persistent inflammatory condition lacking effective therapeutic strategies beyond symptomatic relief. Traditional interventions often fail to address the underlying fibrogenic and immune mechanisms. In recent years, BA has emerged as a promising candidate due to its **anti-inflammatory**, **antioxidant**, and **anti-fibrotic** properties [39, 40]. However, its molecular targets and mechanisms of action in CP have remained poorly defined [19]. Our work identifies the SIRT5-Nrf2 axis as a novel regulatory pathway in CP and provides, to our knowledge, the first evidence that BA exerts its therapeutic effect via modulation of this signaling cascade.

Nrf2 is a well-characterized transcription factor responsible for orchestrating cellular responses to oxidative stress. It has been implicated in diverse inflammatory and fibrotic disorders [11]. Interestingly, the role of Nrf2 in fibrosis seems to vary across pathological contexts. In certain tissues—such as skeletal muscle, liver, and kidney—Nrf2 activation suppresses fibrosis by counteracting oxidative stress and downregulating profibrotic pathways like TGF-β/Smad [41-43]. Conversely, Nrf2 has also been shown to promote fibrogenesis by enhancing fibroblast activation in specific pathological settings [44, 45]. In the pancreas, current literature suggests that Nrf2 plays a predominantly protective role during acute inflammation by reducing oxidative injury and pro-inflammatory cytokine release [46, 47].

In this study, our data reveal a more complex picture in the context of chronic inflammation. Specifically, we observed that Nrf2 expression was elevated in CP tissues, and that silencing Nrf2 in RPDECs *in vitro* significantly enhanced cell viability, reduced apoptosis, and downregulated inflammatory mediators. In *in vivo* CP models, Nrf2 silencing alleviated immune infiltration and pancreatic fibrosis. These results suggest that sustained Nrf2 activation in CP may transition from a protective to a pathogenic role, likely due to aberrant acetylation status, which alters its transcriptional program. This is in stark contrast to the conventional view of Nrf2 as a solely beneficial antioxidant regulator. We propose that, under chronic inflammatory stress, acetylated Nrf2 may perpetuate epithelial injury and immune activation, thereby contributing to fibrotic progression. This highlights the importance of post-translational modifications, such as acetylation, in defining the functional output of Nrf2 signaling.

In recent years, SIRT5 has attracted growing interest for its roles in metabolic regulation and inflammation [48, 49]. While previous studies have primarily associated SIRT5 with oxidative stress modulation, metabolic disorders, and more recently with tumor biology [50, 51], its function in chronic inflammatory diseases has remained largely unexplored. Our study is the first to demonstrate that SIRT5 exerts a regulatory role in CP by controlling the acetylation status of Nrf2. Experimental data confirmed that BA significantly upregulated SIRT5 expression, which led to reduced Nrf2 acetylation and subsequent suppression of the JAK-STAT pathway. These findings not only broaden the known biological functions of SIRT5 beyond metabolism but also identify it as a potential novel therapeutic target in managing chronic inflammatory disorders such as CP.

The JAK-STAT pathway is well-established as a central mediator of chronic inflammation, orchestrating cytokine signaling and immune regulation in a variety of disease contexts [52]. Prior studies have linked overactivation of the JAK-STAT pathway to pancreatic inflammation and fibrosis, with pharmacological inhibition of this axis shown to alleviate CP-like symptoms and reduce fibrotic burden [53, 54]. Our study validates that BA modulates the JAK-STAT pathway indirectly via SIRT5-mediated deacetylation of Nrf2, thereby identifying the SIRT5/Nrf2 axis as an upstream regulator of this key inflammatory pathway. This not only reinforces the pathological relevance of the JAK-STAT signaling in CP but also reveals a previously unrecognized layer of epigenetic regulation involving Nrf2 acetylation.

Another critical aspect of CP progression is immune cell infiltration and T cell differentiation, particularly the skewing toward pro-inflammatory subsets such as Th1 cells. These immune alterations have been associated with heightened inflammation and fibrogenesis in pancreatic tissue [55, 56]. Using FCM and ELISA, our study demonstrates that BA notably reduces immune cell infiltration and shifts T cell differentiation toward anti-inflammatory phenotypes, particularly Th2 cells. This immunomodulatory effect likely contributes to the observed improvements in both inflammatory and fibrotic outcomes. These results not only substantiate the immunological basis of CP pathogenesis but also suggest that BA may hold promise as a candidate immunotherapeutic agent capable of restoring T cell homeostasis in chronic inflammatory conditions.

In our study, a well-established **rat model of CP** was employed to comprehensively evaluate the **therapeutic efficacy of BA** through **histological staining**, **IHC**, and **biochemical assays**. The results demonstrated that BA treatment **significantly attenuated pancreatic fibrosis**, **reduced collagen deposition**, and **inhibited immune cell infiltration**. These *in vivo* findings were consistent with our *in vitro* observations, as BA-treated pancreatic tissues exhibited preserved histoarchitecture, diminished expression of **pro-inflammatory cytokines**, and reduced levels of **fibrotic markers**. Together, these results provide strong experimental support for the therapeutic utility of BA in CP and lay a solid foundation for future translational studies.

Despite the promising efficacy of BA and the elucidation of its mechanism via the SIRT5/Nrf2 axis and JAK-STAT pathway, several issues regarding its clinical translation and safety remain to be addressed. While most preclinical studies report that BA is biocompatible and well-tolerated within therapeutic dose ranges [17], there is evidence suggesting that prolonged use or high doses may induce nephrotoxicity [57]. Furthermore, BA is known to have poor oral bioavailability [58], and its absorption, distribution, metabolism, and excretion profiles require further clarification. Consequently, before BA can be considered for widespread application as a functional food component or adjunct therapeutic agent, it is critical to perform comprehensive toxicological assessments and pharmacokinetic analyses, along with well-designed clinical trials to confirm its long-term safety and therapeutic efficacy in human populations.

In summary, this study identifies a novel SIRT5-Nrf2-JAK/STAT signaling axis as a key pathway modulated by BA to alleviate inflammation and fibrosis in CP. BA exhibited robust therapeutic effects in both cellular and animal models, suggesting its potential as a multifunctional anti-inflammatory agent. Despite the important scientific and clinical implications of this research, some limitations remain. The current findings are based solely on rodent models, and clinical validation in humans is still lacking. Future studies should explore the potential applications of BA in other inflammatory diseases and develop clinical treatment protocols based on BA. Additionally, the role of the SIRT5/Nrf2 signaling axis in other inflammation and metabolism-related diseases warrants further investigation.

5. Conclusion

This study systematically explores the cellular and molecular mechanisms underlying CP progression and demonstrates the therapeutic potential of BA in regulating disease-associated immune and fibrotic responses. scRNA-seq analysis initially identified T cells and epithelial cells as central players in intercellular communication within CP tissues. Notably, Nrf2 expression was significantly elevated in pancreatic tissues from CP patients, implicating it in the regulation of immune responses during disease pathogenesis. Through a combination of *cellular* and *animal* experiments, we showed that **silencing Nrf2** or **administering BA** promoted the **proliferation of RPDECs**, reduced **cellular apoptosis**, and improved **clinical and histological features of CP**, including **suppression of fibrosis**. These interventions also modulated inflammatory mediators by **downregulating pro-inflammatory cytokines** and **upregulating anti-inflammatory cytokines**, thereby attenuating the overall inflammatory response. Additionally, BA treatment inhibited immune cell infiltration in pancreatic tissue and shifted T cell differentiation toward anti-inflammatory subsets, including Th2 and Treg cells, while suppressing the generation of Th1 and Th17 cells.

Integrating high-throughput transcriptomic sequencing with experimental validation, our study revealed that BA exerted these effects by upregulating SIRT5, which in turn reduced Nrf2 acetylation and inhibited the JAK-STAT pathway. This regulatory cascade enhances RPDEC viability, reduces apoptosis, and mitigates inflammation and fibrosis in CP. The proposed SIRT5-Nrf2-JAK/STAT axis offers a novel molecular target for therapeutic intervention (Graphic abstract).

While our findings provide a strong mechanistic basis for the use of BA in CP treatment, some limitations should be noted. First, the therapeutic significance of BA was assessed only in a rat model of CP, and further validation in additional preclinical models and human tissues is essential to confirm translational relevance. Second, although the current study focused on the JAK-STAT pathway, it is plausible that BA may exert broader regulatory effects through other pathways and transcriptional networks. Future research should aim to map BA's full signaling landscape and investigate potential synergistic effects with other therapeutic agents.

Conflict of Interest

The author declares no conflict of interest.

Acknowledgment

None.

Ethical Statement

All animal experiments were approved by the Animal Ethics Committee of The Second Affiliated Hospital of Jiaxing University (No. JUMC2024-109).

Funding

This study was supported by the Project of the Bureau of Science and Technology of Jiaxing City (grant no. 2024AZ30002).

Data Availability

All data generated or analyzed during this study are included in this article and/or its supplementary material files. Further enquiries can be directed to the corresponding author.

References

[1] F. Erchinger, T. Engjom, G. Dimcevski, A.M. Drewes, S.S. Olesen, M. Vujasinovic, J.-M. Löhr, C. Nøjgaard, S. Novovic, J. Laukkarinen, M. Parhiala, L. Björn, A. Waage, T. Hauge, A. Pukitis, I. Ozola-Zalite, E. Kalaitzakis, A. Okhlobystin, G. Barauskas, D. Eva Efsen, E. Tjora, Exocrine pancreas insufficiency in chronic pancreatitis – Risk factors and associations with complications. A multicentre study of 1869 patients, Pancreatology. 22 (2022) 374–380. https://doi.org/10.1016/j.pan.2022.02.003.

[2] M.R. Rickels, A.W. Norris, R.L. Hull, A tale of two pancreases: exocrine pathology and endocrine dysfunction, Diabetologia. 63 (2020) 2030–2039. https://doi.org/10.1007/s00125-020-05210-8.

[3] G. Beyer, A. Habtezion, J. Werner, M.M. Lerch, J. Mayerle, Chronic pancreatitis, The Lancet. 396 (2020) 499–512. https://doi.org/10.1016/s0140-6736(20)31318-0.

[4] P. Campagnola, N. de Pretis, A. Zorzi, F. Caldart, L. Frulloni, Chronic pancreatitis and nutritional support, Best Practice & Research Clinical Gastroenterology. 62–63 (2023) 101823. https://doi.org/10.1016/j.bpg.2023.101823.

[5] U. Jayarajah, T. Widyarathne, M. Nawarathne, S. Raguvaran, N. Subramaniam, R. Riza, I. De Zoysa, S.L. Seneviratne, Clinical characteristics and quality of life among Sri Lankan patients with chronic pancreatitis, J Int Med Res. 48 (2020). https://doi.org/10.1177/0300060520979875.

[6] A. Madro, Malnutrition in Chronic Pancreatitis: Causes, Assessment Methods, and Therapeutic Management, Canadian Journal of Gastroenterology and Hepatology. 2020 (2020) 1–6. https://doi.org/10.1155/2020/8875487.

[7] T.P. Foster, B. Bruggeman, M. Campbell-Thompson, M.A. Atkinson, M.J. Haller, D.A. Schatz, Exocrine Pancreas Dysfunction in Type 1 Diabetes, Endocrine Practice. 26 (2020) 1505–1513. https://doi.org/10.4158/ep-2020-0295.

[8] X. Song, L. Qiao, X. Dou, J. Chang, X. Zeng, T. Deng, G. Yang, P. Liu, C. Wang, Q. Xu, C. Xu, Hypertriglyceridemia-modulated gut microbiota promotes lysophosphatidylcholine generation to aggravate acute pancreatitis in a TLR4-dependent manner, IMeta. 4 (2025). https://doi.org/10.1002/imt2.70003.

[9] L. Swentek, D. Chung, H. Ichii, Antioxidant Therapy in Pancreatitis, Antioxidants. 10 (2021) 657. https://doi.org/10.3390/antiox10050657.

[10] W. Tu, H. Wang, S. Li, Q. Liu, H. Sha, The Anti-Inflammatory and Anti-Oxidant Mechanisms of the Keap1/Nrf2/ARE Signaling Pathway in Chronic Diseases, Aging and Disease. 10 (2019) 637. https://doi.org/10.14336/ad.2018.0513.

[11] L. Kong, H. Zhang, C. Lu, K. Shi, H. Huang, Y. Zheng, Y. Wang, D. Wang, H. Wang, W. Huang, AICAR, an AMP-Activated Protein Kinase Activator, Ameliorates Acute Pancreatitis-Associated Liver Injury Partially Through Nrf2-Mediated Antioxidant Effects and Inhibition of NLRP3 Inflammasome Activation, Front. Pharmacol. 12 (2021). https://doi.org/10.3389/fphar.2021.724514.

[12] J. Yang, X. Tang, X. Ke, Y. Dai, J. Shi, Triptolide Suppresses NF-κB-Mediated Inflammatory Responses and Activates Expression of Nrf2-Mediated Antioxidant Genes to Alleviate Caerulein-Induced Acute Pancreatitis, IJMS. 23 (2022) 1252. https://doi.org/10.3390/ijms23031252.

[13] W.-D. Xu, C. Yang, A.-F. Huang, The role of Nrf2 in immune cells and inflammatory autoimmune diseases: a comprehensive review, Expert Opinion on Therapeutic Targets. 28 (2024) 789–806. https://doi.org/10.1080/14728222.2024.2401518.

[14] Z. Xu, M. Chu, Advances in Immunosuppressive Agents Based on Signal Pathway, Front. Pharmacol. 13 (2022). https://doi.org/10.3389/fphar.2022.917162.

[15] S.K. Law, D.C.T. Au, A review of medicine and food homology on traditional Chinese medicine as functional food, Food & Medicine Homology. (2025). https://doi.org/10.26599/fmh.2026.9420091.

[16] L. Wang, S. Huang, X. Liang, J. Zhou, Y. Han, J. He, D. Xu, Immuno-modulatory role of baicalin in atherosclerosis prevention and treatment: current scenario and future directions, Front. Immunol. 15 (2024). https://doi.org/10.3389/fimmu.2024.1377470.

[17] A. Bajek-Bil, M. Chmiel, A. Włoch, M. Stompor-Gorący, Baicalin—Current Trends in Detection Methods and Health-Promoting Properties, Pharmaceuticals. 16 (2023) 570. https://doi.org/10.3390/ph16040570.

[18] R. Wang, C. Wang, L. Lu, F. Yuan, F. He, Baicalin and baicalein in modulating tumor microenvironment for cancer treatment: A comprehensive review with future perspectives, Pharmacological Research. 199 (2024) 107032. https://doi.org/10.1016/j.phrs.2023.107032.

[19] Y. Wen, Y. Wang, C. Zhao, B. Zhao, J. Wang, The Pharmacological Efficacy of Baicalin in Inflammatory Diseases, IJMS. 24 (2023) 9317. https://doi.org/10.3390/ijms24119317.

[20] Q. Hu, W. Zhang, Z. Wu, X. Tian, J. Xiang, L. Li, Z. Li, X. Peng, S. Wei, X. Ma, Y. Zhao, Baicalin and the liver-gut system: Pharmacological bases explaining its therapeutic effects, Pharmacological Research. 165 (2021) 105444. https://doi.org/10.1016/j.phrs.2021.105444.

[21] Y. Li, K. Song, H. Zhang, M. Yuan, N. An, Y. Wei, L. Wang, Y. Sun, Y. Xing, Y. Gao, Anti-inflammatory and immunomodulatory effects of baicalin in cerebrovascular and neurological disorders, Brain Research Bulletin. 164 (2020) 314–324. https://doi.org/10.1016/j.brainresbull.2020.08.016.

[22] F.S.Ş. Deniz, G. Eren, I.E. Orhan, Flavonoids as Sirtuin Modulators, CTMC. 22 (2022) 790–805. https://doi.org/10.2174/1568026622666220422094744.

[23] H. Xiao, Y. Xie, K. Xi, J. Xie, M. Liu, Y. Zhang, Z. Cheng, W. Wang, B. Guo, S. Wu, Targeting Mitochondrial Sirtuins in Age-Related Neurodegenerative Diseases and Fibrosis, Aging and Disease. 14 (2023) 1583. https://doi.org/10.14336/ad.2023.0203.

[24] Y. Wei, Y. Guo, S. Lv, Research on the progress of Traditional Chinese medicine components and preparations on histone deacetylase inhibitors - Like effects in the course of disease treatment, Journal of Ethnopharmacology. 296 (2022) 115521. https://doi.org/10.1016/j.jep.2022.115521.

[25] L. Kong, X. Xu, H. Zhang, Y. Zhou, H. Huang, B. Chen, Z. Zhou, Human umbilical cord–derived mesenchymal stem cells improve chronic pancreatitis in rats via the AKT-mTOR-S6K1 signaling pathway, Bioengineered. 12 (2021) 1986–1996. https://doi.org/10.1080/21655979.2021.1928441.

[26] J. Li, Y. Wu, S. Zhang, J. Zhang, F. Ji, W. Bo, X. Guo, Z. Li, Baicalein protect pancreatic injury in rats with severe acute pancreatitis by inhibiting pro-inflammatory cytokines expression, Biochemical and Biophysical Research Communications. 466 (2015) 664–669. https://doi.org/10.1016/j.bbrc.2015.09.094.

[27] Y.-T. Huang, Q.-Q. Liang, H.-R. Zhang, S.-Y. Chen, L.-H. Xu, B. Zeng, R. Xu, F.-L. Shi, D.-Y. Ouyang, Q.-B. Zha, X.-H. He, Baicalin inhibits necroptosis by decreasing oligomerization of phosphorylated MLKL and mitigates caerulein-induced acute pancreatitis in mice, International Immunopharmacology. 108 (2022) 108885. https://doi.org/10.1016/j.intimp.2022.108885.

[28] D. Yan, A. Franzini, A.D. Pomicter, B.J. Halverson, O. Antelope, C.C. Mason, J.M. Ahmann, A.V. Senina, N.A. Vellore, C.L. Jones, M.S. Zabriskie, H. Than, M.J. Xiao, A. van Scoyk, A.B. Patel, P.M. Clair, W.L. Heaton, S.C. Owen, J.L. Andersen, C.M. Egbert, J.A. Reisz, A. D'Alessandro, J.E. Cox, K.C. Gantz, H.M. Redwine, S.M. Iyer, J.S. Khorashad, N. Rajabi, C.A. Olsen, T. O'Hare, M.W. Deininger, SIRT5 Is a Druggable Metabolic Vulnerability in Acute Myeloid Leukemia, Blood Cancer Discovery. 2 (2021) 266–287. https://doi.org/10.1158/2643-3230.bcd-20-0168.

[29] X. Sun, Z. Xie, B. Hu, B. Zhang, Y. Ma, X. Pan, H. Huang, J. Wang, X. Zhao, Z. Jie, P. Shi, Z. Chen, The Nrf2 activator RTA-408 attenuates osteoclastogenesis by inhibiting STING dependent NF-κb signaling, Redox Biology. 28 (2020) 101309. https://doi.org/10.1016/j.redox.2019.101309.

[30] V.K. Singh, D. Yadav, P.K. Garg, Diagnosis and Management of Chronic Pancreatitis, JAMA. 322 (2019) 2422. https://doi.org/10.1001/jama.2019.19411.

[31] J.M. Braganza, S.H. Lee, R.F. McCloy, M.J. McMahon, Chronic pancreatitis, The Lancet. 377 (2011) 1184–1197. https://doi.org/10.1016/s0140-6736(10)61852-1.

[32] R. Mann, U. Boregowda, N. Vyas, M. Gajendran, C.P. Umapathy, H. Sayana, J. Echavarria, S. Patel, S. Saligram, Current advances in the management of chronic pancreatitis, Disease-a-Month. 67 (2021) 101225. https://doi.org/10.1016/j.disamonth.2021.101225.

[33] Histol Histopathol, Vol 39, Yang et al., (n.d.). https://doi.org/10.14670/HH-18-733.

[34] X. Wang, H. Cai, Z. Chen, Y. Zhang, M. Wu, X. Xu, L. Yang, Baicalein alleviates pyroptosis and inflammation in hyperlipidemic pancreatitis by inhibiting NLRP3/Caspase-1 pathway through the miR-192-5p/TXNIP axis, International Immunopharmacology. 101 (2021) 108315. https://doi.org/10.1016/j.intimp.2021.108315.

[35] W. Pu, R. Bai, K. Zhou, Y. Peng, M. Zhang, M.O. Hottiger, W. Li, X. Gao, L. Sun, Baicalein attenuates pancreatic inflammatory injury through regulating MAPK, STAT 3 and NF-κB activation, International Immunopharmacology. 72 (2019) 204–210. https://doi.org/10.1016/j.intimp.2019.04.018.

[36] M. Chen, J. Tan, Z. Jin, T. Jiang, J. Wu, X. Yu, Research progress on Sirtuins (SIRTs) family modulators, Biomedicine & Pharmacotherapy. 174 (2024) 116481. https://doi.org/10.1016/j.biopha.2024.116481.

[37] J. Sun, J. Cai, J. Chen, S. Li, X. Liao, Y. He, X. Chen, S. Hu, Krüppel-Like Factor 6 Silencing Prevents Oxidative Stress and Neurological Dysfunction Following Intracerebral Hemorrhage via Sirtuin 5/Nrf2/HO-1 Axis, Front. Aging Neurosci. 13 (2021). https://doi.org/10.3389/fnagi.2021.646729.

[38] X. Sun, S. Wang, J. Gai, J. Guan, J. Li, Y. Li, J. Zhao, C. Zhao, L. Fu, Q. Li, SIRT5 Promotes Cisplatin Resistance in Ovarian Cancer by Suppressing DNA Damage in a ROS-Dependent Manner via Regulation of the Nrf2/HO-1 Pathway, Front. Oncol. 9 (2019). https://doi.org/10.3389/fonc.2019.00754.

[39] Z. Hu, Y. Guan, W. Hu, Z. Xu, M. Ishfaq, An overview of pharmacological activities of baicalin and its aglycone baicalein: New insights into molecular mechanisms and signaling pathways, Iranian Journal of Basic Medical Sciences. 25 (2022) 14–26. https://doi.org/10.22038/ijbms.2022.60380.13381.

[40] M. Chang, W. Chen, R. Xia, Y. Peng, P. Niu, H. Fan, Pancreatic Stellate Cells and the Targeted Therapeutic Strategies in Chronic Pancreatitis, Molecules. 28 (2023) 5586. https://doi.org/10.3390/molecules28145586.

[41] H. Wang, B. Wang, J. Wei, Z. Zheng, J. Su, C. Bian, Y. Xin, X. Jiang, Sulforaphane regulates Nrf2-mediated antioxidant activity and downregulates TGF-β1/Smad pathways to prevent radiation-induced muscle fibrosis, Life Sciences. 311 (2022) 121197. https://doi.org/10.1016/j.lfs.2022.121197.

[42] M.-K. Song, J.-H. Lee, I. Ryoo, S. Lee, S.-K. Ku, M.-K. Kwak, Bardoxolone ameliorates TGF-β1-associated renal fibrosis through Nrf2/Smad7 elevation, Free Radical Biology and Medicine. 138 (2019) 33–42. https://doi.org/10.1016/j.freeradbiomed.2019.04.033.

[43] Z. Wang, P. Sun, T. Zhao, J. Cao, Y. Liu, A. Khan, W. Zhou, G. Cheng, E Se tea extract ameliorates CCl4 induced liver fibrosis via regulating Nrf2/NF-κB/TGF-β1/Smad pathway, Phytomedicine. 115 (2023) 154854. https://doi.org/10.1016/j.phymed.2023.154854.

[44] J.I. Kang, D.H. Kim, K.W. Sung, S.M. Shim, H. Cha-Molstad, N.K. Soung, K.H. Lee, J. Hwang, H.G. Lee, Y.T. Kwon, B.Y. Kim, p62-Induced Cancer-Associated Fibroblast Activation via the Nrf2-ATF6 Pathway Promotes Lung Tumorigenesis, Cancers. 13 (2021) 864. https://doi.org/10.3390/cancers13040864.

[45] B. C. de S. Ribeiro, R. V. de C. Faria, J. de S. Nogueira, S. Santos Valença, L. Chen, B. Romana-Souza, Olive oil promotes the survival and migration of dermal fibroblasts through Nrf2 pathway activation, Lipids. 58 (2022) 59–68. https://doi.org/10.1002/lipd.12363.

[46] M.J. Rodríguez, M. Sabaj, G. Tolosa, F. Herrera Vielma, M.J. Zúñiga, D.R. González, J. Zúñiga-Hernández, Maresin-1 Prevents Liver Fibrosis by Targeting Nrf2 and NF-κB, Reducing Oxidative Stress and Inflammation, Cells. 10 (2021) 3406. https://doi.org/10.3390/cells10123406.

[47] X. Liang, M. Han, X. Zhang, X. Sun, K. Yu, C. Liu, J. Zhang, C. Hu, J. Zhang, Dahuang Danshen Decoction Inhibits Pancreatic Fibrosis by Regulating Oxidative Stress and Endoplasmic Reticulum Stress, Evidence-Based Complementary and Alternative Medicine. 2021 (2021) 1–12. https://doi.org/10.1155/2021/6629729.

[48] M. Kitada, Y. Ogura, I. Monno, D. Koya, Sirtuins and Type 2 Diabetes: Role in Inflammation, Oxidative Stress, and Mitochondrial Function, Front. Endocrinol. 10 (2019). https://doi.org/10.3389/fendo.2019.00187.

[49] W.H. almalki, A. Alzahrani, M.E.-S. Mahmoud El-Daly, A.-S.H.F. Fadel Ahmed, The emerging potential of SIRT-3 in oxidative stress-inflammatory axis associated increased neuroinflammatory component for metabolically impaired neural cell, Chemico-Biological Interactions. 333 (2021) 109328. https://doi.org/10.1016/j.cbi.2020.109328.

[50] E. Fabbrizi, F. Fiorentino, V. Carafa, L. Altucci, A. Mai, D. Rotili, Emerging Roles of SIRT5 in Metabolism, Cancer, and SARS-CoV-2 Infection, Cells. 12 (2023) 852. https://doi.org/10.3390/cells12060852.

[51] Z. Pan, H. Dong, N. Huang, J. Fang, Oxidative stress and inflammation regulation of sirtuins: New insights into common oral diseases, Front. Physiol. 13 (2022). https://doi.org/10.3389/fphys.2022.953078.

[52] H.-T. Tzeng, I.-T. Chyuan, J.-H. Lai, Targeting the JAK-STAT pathway in autoimmune diseases and cancers: A focus on molecular mechanisms and therapeutic potential, Biochemical Pharmacology. 193 (2021) 114760. https://doi.org/10.1016/j.bcp.2021.114760.

[53] G. Jin, W. Hong, Y. Guo, Y. Bai, B. Chen, Molecular Mechanism of Pancreatic Stellate Cells Activation in Chronic Pancreatitis and Pancreatic Cancer, J. Cancer. 11 (2020) 1505–1515. https://doi.org/10.7150/jca.38616.

[54] H.-L. Guo, X.-S. Liang, X.-P. Zeng, Y. Liu, Z.-S. Li, L.-J. Wang, L.-H. Hu, Pirfenidone alleviates chronic pancreatitis via suppressing the activation of pancreatic stellate cells and the M1 polarization of macrophages, International Immunopharmacology. 130 (2024) 111691. https://doi.org/10.1016/j.intimp.2024.111691.

[55] J. Glaubitz, A. Wilden, C. van den Brandt, F.U. Weiss, B.M. Bröker, J. Mayerle, M.M. Lerch, M. Sendler, Experimental pancreatitis is characterized by rapid T cell activation, Th2 differentiation that parallels disease severity, and improvement after CD4+ T cell depletion, Pancreatology. 20 (2020) 1637–1647. https://doi.org/10.1016/j.pan.2020.10.044.

[56] J. Glaubitz, A. Wilden, J. Golchert, G. Homuth, U. Völker, B.M. Bröker, T. Thiele, M.M. Lerch, J. Mayerle, A.A. Aghdassi, F.U. Weiss, M. Sendler, In mouse chronic pancreatitis CD25+FOXP3+ regulatory T cells control pancreatic fibrosis by suppression of the type 2 immune response, Nat Commun. 13 (2022). https://doi.org/10.1038/s41467-022-32195-2.

[57] loading, (n.d.). https://doi.org/10.3760/cma.j.cn121094-20200326-00158.

[58]C. Liu, W. Du, L. Zhang, J. Wang, Natural synergy: Oleanolic acid-curcumin co-assembled nanoparticles combat osteoarthritis, Colloids and Surfaces B: Biointerfaces. 245 (2025) 114286. https://doi.org/10.1016/j.colsurfb.2024.114286.